Cell Reports

Article

Architectural organization of ~1,500-neuron modular minicolumnar disinhibitory circuits in healthy and Alzheimer's cortices

Graphical abstract

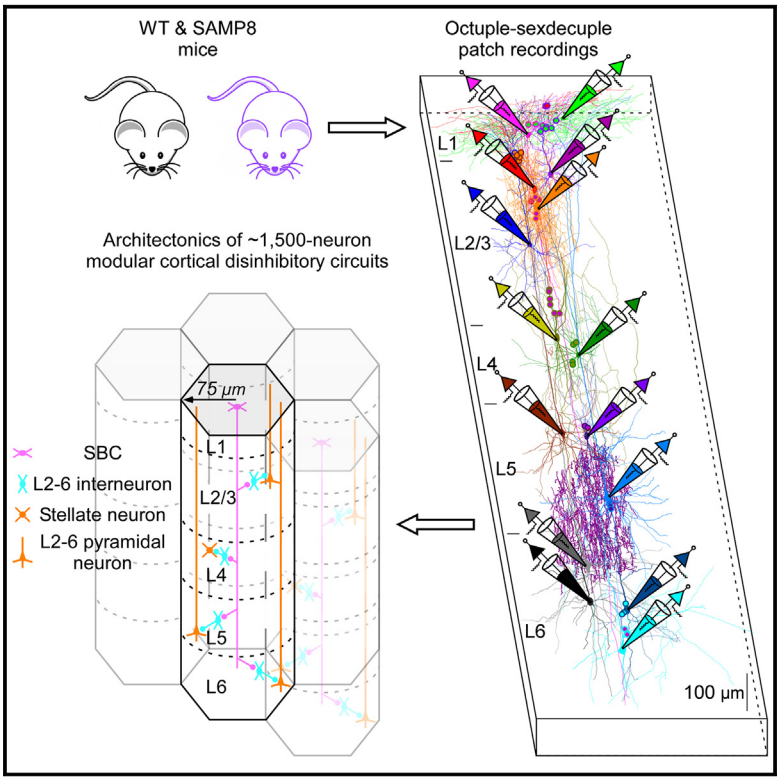

Authors

J. Julius Zhu

Correspondence

jjzhu@virginia.edu

In brief

Zhu introduced an octuple-sexdecuple patch-clamp recording technique, allowing for the architectural reconstruction of cortical L1 SBC-led modular circuits featuring translaminar, unidirectional, minicolumnar, and independent disinhibition. The architectures construe cortical operational principles and circuit- and connection-specific deficits at SBC-disinhibited synapses in the SAMP8 mouse, an Alzheimer's disease model.

Highlights

- Octuple-sexdecuple patch recordings enable architectonics of complex cortical circuits
- Architectonics identifies modular L1 SBC-led disinhibitory circuits across cortices
- Architectures of L1 SBC-led disinhibitory circuits construe principles of cortical operation
- Architectonics reveals specific deficits at SBC-disinhibited synapses in an AD mouse model

Zhu, 2023, Cell Reports *42*, 112904
August 29, 2023
https://doi.org/10.1016/j.celrep.2023.112904

CellPress

Cell Reports

CellPress
OPEN ACCESS

Article

Architectural organization of ~1,500-neuron modular minicolumnar disinhibitory circuits in healthy and Alzheimer's cortices

J. Julius Zhu[1,2,3,4,*]
[1]Kavli Institute for Systems Neuroscience, Norwegian University of Science and Technology, 7491 Trondheim, Norway
[2]Department of Neurophysiology, Donders Institute for Brain, Cognition and Behavior, Radboud University, 6500 GL Nijmegen, the Netherlands
[3]Departments of Pharmacology and Neuroscience, University of Virginia School of Medicine, Charlottesville, VA 22908, USA
[4]Lead contact
*Correspondence: jjzhu@virginia.edu
https://doi.org/10.1016/j.celrep.2023.112904

SUMMARY

Acquisition of neuronal circuit architectures, central to understanding brain function and dysfunction, remains prohibitively challenging. Here I report the development of a simultaneous and sequential octuple-sexdecuple whole-cell patch-clamp recording system that enables architectural reconstruction of complex cortical circuits. The method unveils the canonical layer 1 single bouquet cell (SBC)-led disinhibitory neuronal circuits across the mouse somatosensory, motor, prefrontal, and medial entorhinal cortices. The ~1,500-neuron modular circuits feature the translaminar, unidirectional, minicolumnar, and independent disinhibition and optimize cortical complexity, subtlety, plasticity, variation, and redundancy. Moreover, architectural reconstruction uncovers age-dependent deficits at SBC-disinhibited synapses in the senescence-accelerated mouse prone 8, an animal model of Alzheimer's disease. The deficits exhibit the characteristic Alzheimer's-like cortical spread and correlation with cognitive impairments. These findings decrypt operations of the elementary processing units in healthy and Alzheimer's mouse cortices and validate the efficacy of octuple-sexdecuple patch-clamp recordings for architectural reconstruction of complex neuronal circuits.

INTRODUCTION

The sustained interest in neuronal circuits stems from the belief that intricately organized circuits provide the foundation for brain function.[1,2] In the past decade, significant progress has been made in our ability to decipher these circuits at the synaptic level with cell-type specificity, thanks to advancements in anatomic, neurophysiological, genetic, and functional imaging methods.[3,4] These technical advances have allowed for cell-type-specific circuit analysis, enabling researchers to decode hundreds of functional neuronal circuit motifs, consisting typically of a few different types of neurons, in various animal species. Among the various newly identified circuit motifs are the layer 1 (L1) single bouquet cell (SBC)-led disinhibitory neuronal circuit motifs (i.e., L1 interneurons —• L2/3 interneurons —• L2/3 and/or L5 pyramidal neurons) found in the cortex, which disclose a disinhibition scheme that governs the dendritic coincidence detection mechanism of excitatory neurons and their outputs.[5,6] This cortical disinhibition mechanism has been implicated in various high cognitive behaviors, such as perception, attention, learning, and memory.[7–12] However, understanding the higher-order circuit organization scheme and the overall architectural structure of complex circuits, which involve a large number of neurons and multiple circuit motifs, remains extremely challenging. For example, although optogenetics and functional imaging are effective in determining synaptic connections between neuronal groups, the methods are less suitable for zoom-in manipulation of compactly packed individual neurons to tease out the interconnections of neurons and to figure out the circuit architectural organization.[3,4] High-speed scanning electron microscopy permits high-resolution analysis of pre- and postsynaptic components, but the process of stitching and aligning miniature image sections to create a zoom-out interlinking diagram of individual neurons or circuit motifs and to see the circuit architectural design is still a daunting task.[13,14] While these approaches evolve rapidly and become increasingly more powerful in illuminating the fine details of circuit motifs,[14–16] they have yet to fully resolve the overall architectural structure of complex cortical circuits. As a result, we still have a paltry sense of architectural designs of complex cortical circuits, which are almost certainly at the heart of their operation and function.[1,2]

This study describes the development of a simultaneous and sequential octuple-sexdecuple whole-cell patch-clamp recording system, which allows for direct manipulation and readout from individual neurons. The electrophysiology-based

method offers the advantage of analyzing interconnections between a sufficient number of circuit elements (i.e., neurons and associated circuit motifs) to achieve the architectural reconstruction of complex cortical circuits. In the field of connectomics, many investigators use molecular markers to identify and classify neurons. This approach is convenient and genetically manipulable. However, it is important to consider that genetically defined cortical cell groups display a continuum of variability in morphology and electrophysiology, which means they may not represent biological or functional discrete entities.[17,18] In particular, caution should be exercised when analyzing cortical interneuronal circuits based on four coarse molecular subgroups, all of which consist of multiple overlapping types of interneurons. For example, parvalbumin-expressing neurons consist of at least baskets cells (BCs) and chandelier cells (ChCs).[19,20] Somatostatin-expressing neurons comprise both Martinotti cells (MCs) and non-Martinotti cells.[21–24] Vasointenstinal protein (VIP)-expressing neurons are heterogeneous groups of interneurons that encompass bituft cells (BTCs), bipolar cells (BPCs), BCs, and double bouquet cells (DBCs), and may or may not include L1 SBCs.[25–27] Finally, newly designated Id2-expressing neurons correspond to elongated neurogliaform cells (ENGCs) in L1, and neurogliaform cells (NGCs) and a small number of diverse non-NGCs outside L1.[28] This study uses the established neuroanatomical cell classification scheme to identify cortical neurons because electrophysiology allows morphological reconstruction of >95% of neurons after patch-clamp recordings. In the case of inhibitory neurons, the scheme is based purely on their axonal morphology corresponding to their postsynaptic compartment targets and is thus presumably functionally relevant.[5,19,29–31]

This study analyzed interconnections of morphologically identified 6,517 interneurons and 9,089 stellate and pyramidal neurons in the mouse somatosensory, motor, prefrontal, and medial entorhinal cortices. The analysis disclosed the modular architectural structure of complex L1 SBC-led disinhibitory neuronal circuits across the cortical areas. The architectural structure indicates that the circuits are specifically designed to achieve the distinctive translaminar (engaging all cortical layers), unidirectional (creating 100% dominance), minicolumnar (enclosing area of ~150 μm in diameter), and independent (forming 100% autonomy) disinhibition. The architectures immediately construe the principles underlying cortical operation. One key principle is that cortical operation utilizes canonical ~1,500-neuron minicolumnar circuits as basic functional units to optimize complexity, subtlety, plasticity, variation, and redundancy. Additionally, the study investigated the senescence-accelerated mouse prone 8, an Alzheimer's disease model, and validated the architectural design of the disinhibitory circuits. Interestingly, the architectural analysis of complex cortical circuits in Alzheimer's mouse brains revealed age-dependent deficits. The deficits were circuit- and connection-specific and occurred selectively at SBC-disinhibited synapses. These synaptic deficits displayed the characteristic cortical spread observed in Alzheimer's disease and showed correlations with cognitive impairments. The results suggest a disinhibition mechanism that may contribute to the development and progression of Alzheimer's disease.

RESULTS

To interrogate complex cortical circuits comprising ≥10 types of neurons and multiple circuit motifs, we developed a simultaneous and sequential octuple-sexdecuple whole-cell patch-clamp recording method. Our approach combined automated procedural algorithms for electrode positioning with manual operation to achieve precise gigasealing (see STAR Methods). By utilizing automatic algorithms, we achieved high-efficiency recordings, reducing the time to obtain individual cell recordings to ~3–5 min (cf. Kodandaramaiah et al.[32]). In the meantime, by making manual gigasealing procedure, we achieved high-quality recordings, preserving the high success rate of first-grade whole-cell recordings from interneurons (>95%), and stellate and pyramidal neurons (>99%) (cf. Jiang et al.[5,6]). The octuple-sexdecuple patch-clamp recording method allowed us to effectively study constituent neurons across six cortical layers in complex cortical circuits, as well as investigate synaptic connections among recorded neurons (see Figure 1 as an example).

Basic properties of a complex L1 SBC-led disinhibitory circuit

The initial application of octuple-sexdecuple patch-clamp recordings reconstructed sufficient elements, including neurons and their connections, leading to a connection diagram of the L1 SBC-led disinhibitory circuit in the mouse somatosensory cortex (Figures 1A–1C). Morphological reconstruction of recorded neurons revealed putative synaptic contacts under light microscopic examination, confirming the connection diagram disclosed by electrophysiological recordings (cf. Jiang et al.[5,6]). The analysis revealed that L1 SBCs inhibited interneurons in deeper cortical layers from L2 to L6, but none of stellate and pyramidal neurons in these layers (Figures 1C–1E). Moreover, the inhibited L2-6 interneurons inhibited a significant proportion of L2-6 stellate and pyramidal neurons (Figures 2A–2C). These results indicate that L1 SBCs establish translaminar disinhibition on stellate and pyramidal neurons across the deeper cortical layers through L2-6 interneurons.

Further analysis revealed the executing direction of L1 SBC-led disinhibitory circuits. While SBCs inhibited all groups of interneurons in L2-6, none of the L2-6 interneurons inhibited SBCs (Figures 2A–2C). In comparison, L1 ENGCs inhibited L1 SBCs (Figures 2A–2C), whereas none of SBCs inhibited ENGCs (Figures 1C–1E). These results indicate that L1 SBCs form unidirectional inhibition on L2-6 interneurons, without receiving any reciprocal inhibition back from L2-6 interneurons. These findings suggest that L1 SBC-led disinhibitory circuits, unlike VIP-containing interneuron-mediated more mutual inhibitory-like circuits,[33] predominantly execute dominative unidirectional disinhibition on excitatory neurons.

The majority of L2-6 interneurons inhibited by L1 SBCs were found within small columnar regions surrounding the SBCs (Figures 1D and 1E). Mapping the location of SBC-inhibited L2-6 interneurons, as well as SBC-disinhibited L2-6 stellate and pyramidal neurons, revealed that these inhibitory and excitatory neurons were primarily confined to narrow circular columnar areas with a radius of ~75 μm. The SBCs were

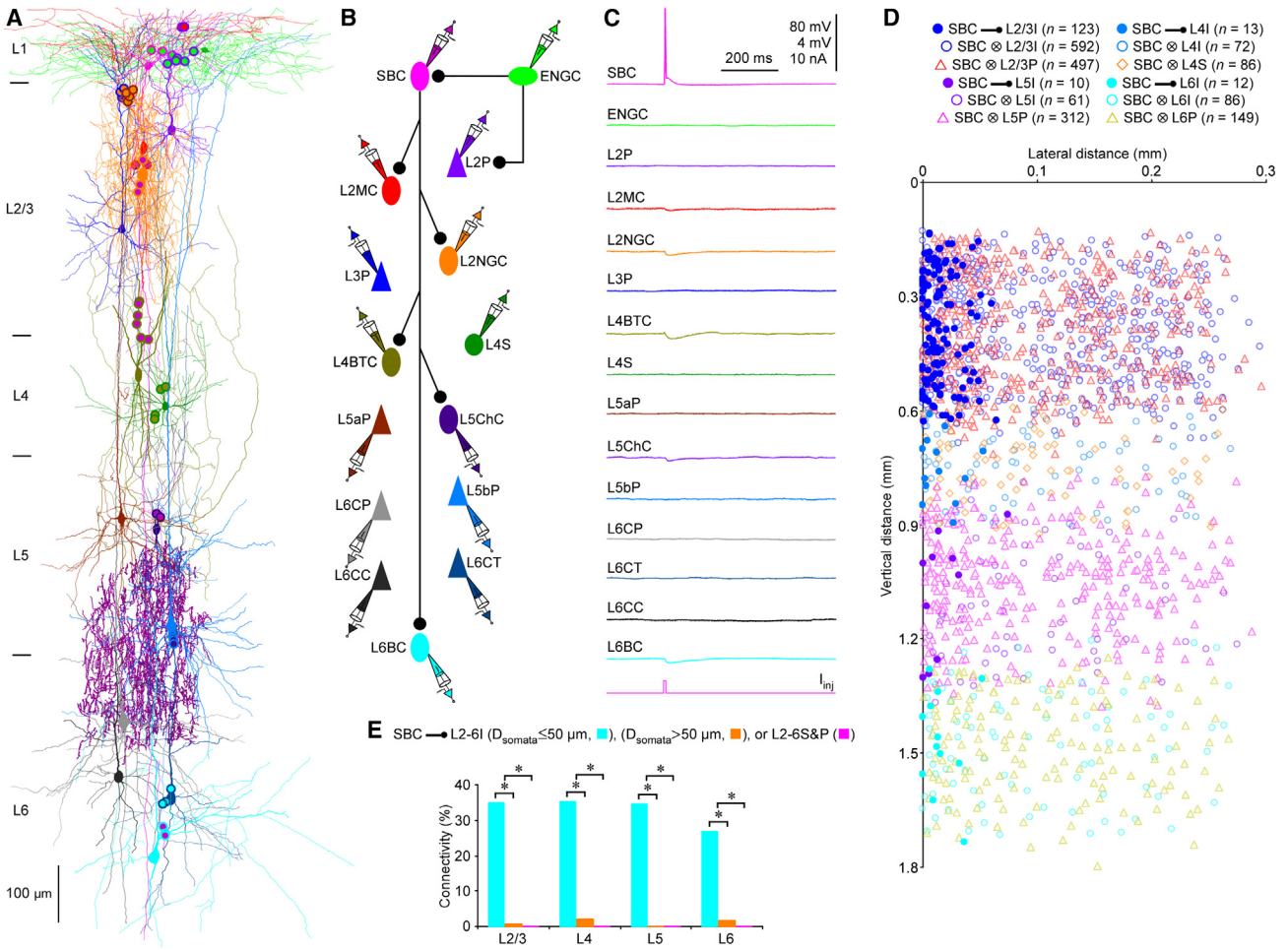

Figure 1. L1 SBCs lead translaminar disinhibitory circuits

(A) Reconstruction of L1 SBC (pink), ENGC (green), and multiple L2-6 interneurons, stellate, and pyramidal neurons recorded simultaneously from a mouse acute somatosensory cortical slice. The double colored dots indicate putative synaptic contacts.

(B) The schematic shows inhibitory synaptic connections.

(C) Single action potentials elicited in presynaptic SBC evoked uIPSPs in postsynaptic L2-6 interneurons, but not stellate or pyramidal neurons. Scale bars apply to all recording traces.

(D) The plot shows relative distances from L2-6 interneurons, stellate, and pyramidal neurons to SBCs (horizontal distance in the x axis) and the cortical pia surface (vertical distance in the y axis). Note filled and empty dots (interneurons), diamonds (stellate neurons), or triangles (pyramidal neurons) representing connected and unconnected neurons, respectively.

(E) Values for the connectivity between SBC and L2-6 interneurons, stellate, or pyramidal neurons in the somatosensory cortex. Asterisks indicate $p < 0.05$ (chi-squared tests). BC, basket cell; BTC, bitufted cell; CC, corticocortical neuron; ChC, chandelier cells; CP, claustrum-projecting neuron; CT, corticothalamic neuron; ENGC, elongated neurogliaform cell; I, interneuron; MC, Martinotti cell; NGC, neurogliaform cell; P, pyramidal neuron; S, stellate neuron; SBC, single bouquet cell.

Note —● and ⊗ in (D) and (E) represent synaptic connection and no connection, respectively.

positioned at the top centers of these columnar areas (Figures 1D, 1E, and 2D–2F). These findings demonstrate that L1 SBCs establish columnar or minicolumnar-like disinhibition on cortical L2-6 excitatory neurons through the involvement of L2-6 interneurons.

Independence of complex L1 SBC-led disinhibitory circuits

The functional relationship between cortical minicolumns has not been previously explored in research.[34,35] By employing octuple-sexdecuple patch-clamp recordings, we greatly increased the probability of obtaining simultaneous recordings from pairs of L1 SBC-led disinhibitory circuits. This allowed us to investigate whether minicolumnar circuits share common circuit elements (Figure 3). The results demonstrated that simultaneously recorded L1 SBCs inhibited L2-6 interneurons, which in turn inhibited L2-6 stellate and pyramidal neurons located within narrow columnar regions beneath the SBCs. These observations confirm the expected characteristics of translaminar, unidirectional, and minicolumnar disinhibitory circuits (Figures 3A–3F).

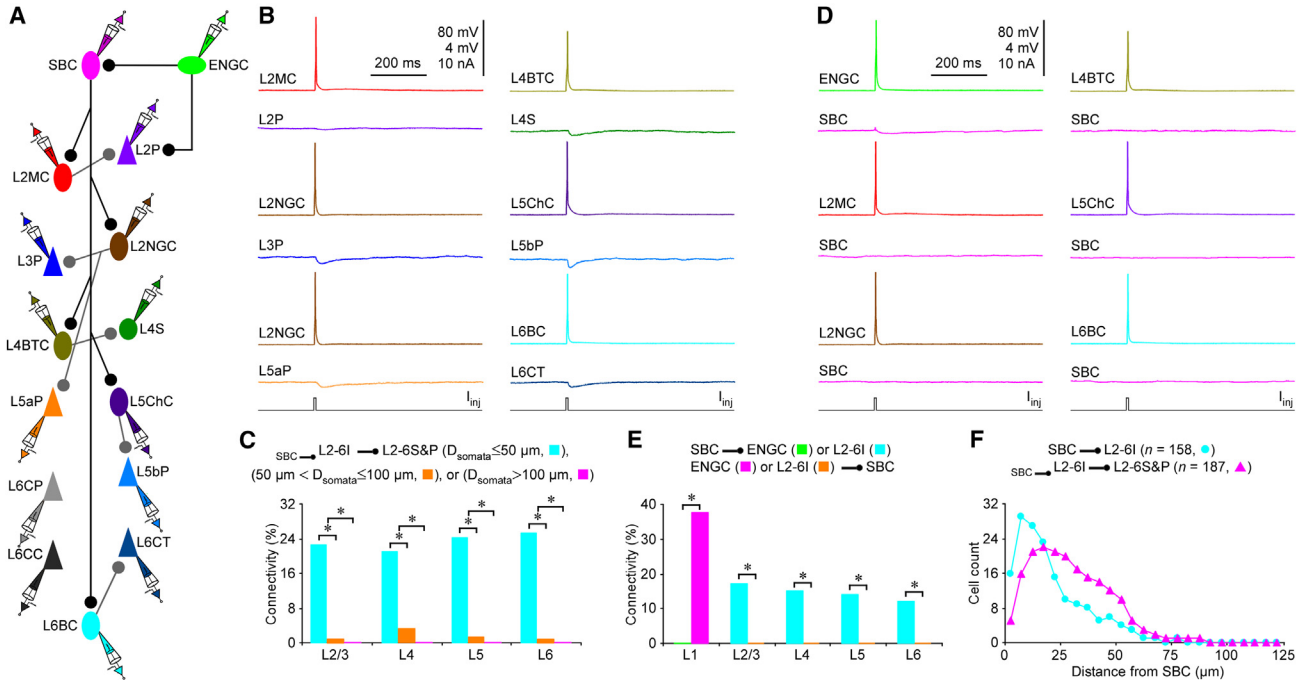

Figure 2. L1 SBCs lead unidirectional and minicolumnar disinhibitory circuits

(A) The schematic shows inhibitory and disinhibitory synaptic connections of neurons reported in Figure 1.

(B) Single action potentials elicited in presynaptic L2-6 interneurons evoked uIPSPs in L2-6 stellate and pyramidal neurons.

(C) Values for the connectivity between SBC-inhibited L2-6 interneurons and L2-6 stellate or pyramidal neurons.

(D) Single action potentials elicited in presynaptic ENGC, but not L2-6 interneurons evoked uIPSPs in SBC. Scale bars in (B) and (D) apply to all recording traces.

(E) Values for the connectivity between SBCs and ENGCs or L2-6 interneurons. Asterisks in (C) and (E) indicate $p < 0.05$ (chi-squared tests).

(F) Lateral distributions of SBC-inhibited L2-6 interneurons and SBC-disinhibited L2-6 stellate or pyramidal neurons.

Note —● in (C), (E), and (F) represent synaptic connection.

Interestingly, L2-6 interneurons, stellate, and pyramidal neurons involved in one L1 SBC-led disinhibitory circuit participated into neither inhibition nor disinhibition of the other disinhibitory circuit (Figures 3G and 3H). Collectively, these results indicate that L1 SBCs establish translaminar, unidirectional, minicolumnar, and independent disinhibition on cortical L2-6 excitatory neurons through the involvement of L2-6 interneurons in the somatosensory cortex.

Modularity of complex L1 SBC-led disinhibitory circuits

The modular architecture of L1 SBC-led disinhibitory circuits in the somatosensory cortex provides the long-sought neuronal circuit basis supporting the "minicolumnar cortical architecture" theory, which purports the existence of translaminar and minicolumnar neuronal circuits in heterotypical cortical areas.[36] Previous studies report that L1 SBCs mediate disinhibition in the motor cortex[5,6] and disinhibition appears to exist in the other cortical areas, including the prefrontal cortex.[37] Octuple-sexdecuple patch-clamp recordings revealed that L1 SBCs inhibited interneurons in L2-6 without being inhibited by L2-6 interneurons in the motor and prefrontal cortex (Figures 4A–4C, 4E–4G, S1, and S2). Furthermore, while L1 SBCs did not inhibit any pyramidal neurons in L2-6, the L1 SBC-inhibited L2-6 interneurons inhibited pyramidal neurons in the motor and prefrontal cortex (Figures 4A–4C, 4E–4G, S1, and S2). Control experiments demonstrated that L1 ENGCs could inhibit SBCs, but SBCs did not inhibit ENGCs in the motor and prefrontal cortex (Figures 4A–4C, 4E–4G, S1, and S2). Additionally, L1 SBC-inhibited interneurons and -disinhibited L2-6 pyramidal neurons were largely confined within narrow columnar areas of ~75 μm in radius (Figures 4C, 4D, 4G–4H, S1, and S2). These results indicate that L1 SBC-led disinhibitory circuits in the motor and prefrontal cortex exhibit the same translaminar, unidirectional, and minicolumnar disinhibition seen in the somatosensory cortex, suggesting a generalized architectural design for L1 SBC-led disinhibitory circuits across the neocortex.

The medial entorhinal cortex, which acts as an interface between the hippocampus and neocortex, is involves in spatial navigation and memory.[40] Interestingly, as with the neocortex, the medial entorhinal cortex also displays a minicolumnar-like anatomical structure,[41] employs two coincident mechanisms for the generation of grid cell firing patterns,[42] and possesses hallmark L1 SBCs and ENGCs (Figure S3, see also Shi et al.[43]). Octuple-sexdecuple patch-clamp recordings revealed the presence of L1 SBC-led disinhibitory circuits in the medial entorhinal cortex (Figures 4I–4K and S4). These circuits involved entorhinal L1 SBCs disinhibiting L2-6 stellate and pyramidal neurons through the participation of L2-6 interneurons, while no inhibitory feedback from L2-6 interneurons to SBCs was observed

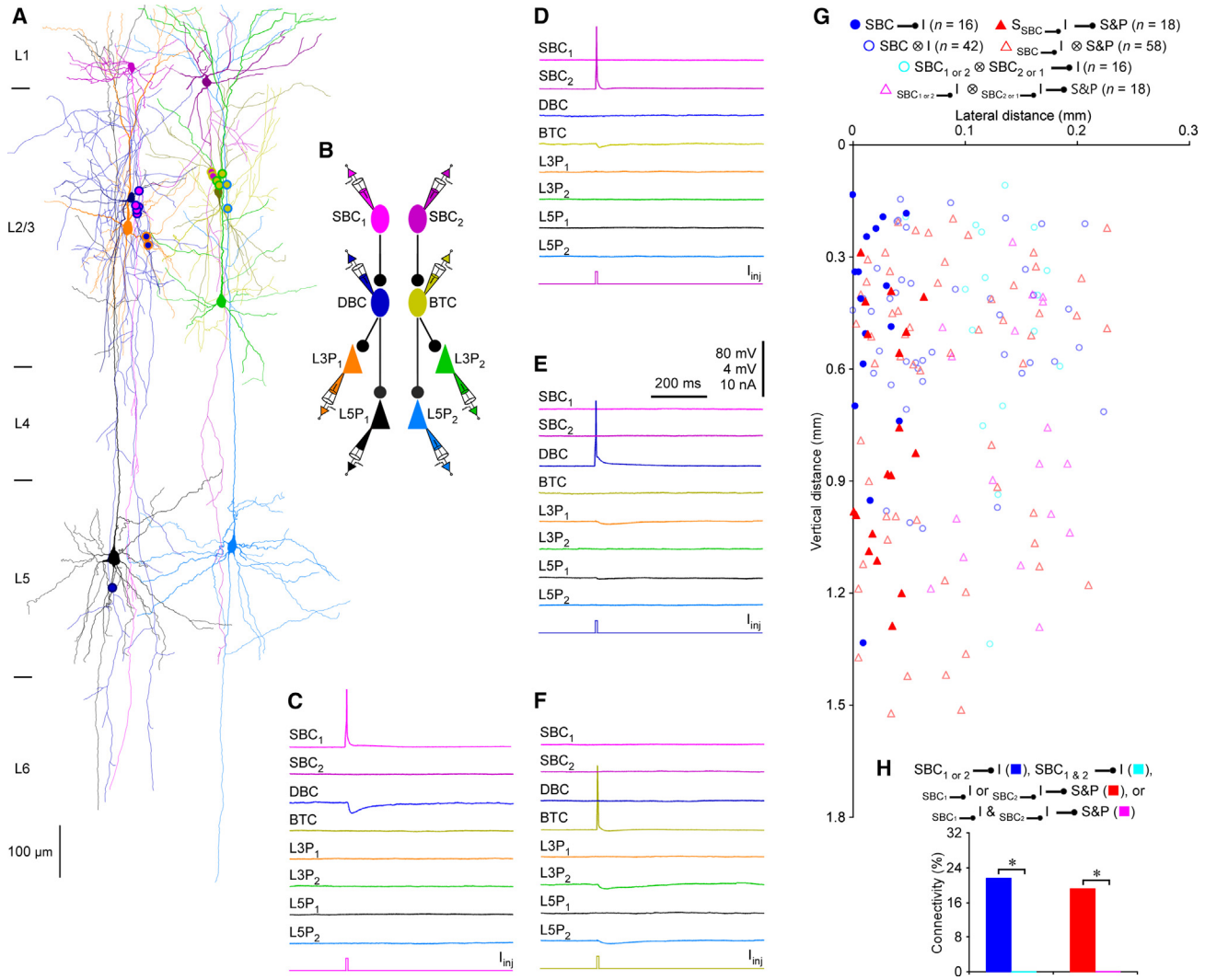

Figure 3. L1 SBCs lead independent disinhibitory circuits

(A) Reconstruction of two L1 SBC-led disinhibitory circuits in a mouse acute somatosensory cortical slice. The double colored dots indicate putative synaptic contacts. Note that for the simplicity, one interneuron and four pyramidal neurons recorded in the experiment but uninvolved in the disinhibitory circuits are excluded in the drawing.

(B) The schematic shows synaptic connections.

(C–F) Single action potentials elicited in presynaptic SBCs and L2 interneurons evoked uIPSPs in postsynaptic L2/3 interneurons, or postsynaptic L2 or L5 pyramidal neurons only within the same SBC-led disinhibitory circuits. Scale bars in (E) apply to all recording traces in (C)–(F). DBC, double bouquet cell; for other abbreviations, please see Figure 1.

(G) The plot shows relative distances from L2-6 interneurons, stellate, and pyramidal neurons to SBCs (horizontal distance in the x axis) and the cortical pia surface (vertical distance in the y axis). Note filled and empty dots (interneurons) or triangles (stellate and pyramidal neurons) represent connected and unconnected neurons, respectively.

(H) Values for the connectivity between SBC and L2-6 interneurons, stellate, or pyramidal neurons involved in the same or different L1 SBC-led disinhibitory circuits. Asterisks indicate $p < 0.05$ (chi-squared tests). Note the average distance of pair-recorded SBCs to be 134.0 ± 8.7 µm (n = 8).

Note —● and ⊗ in (G) and (H) represent synaptic connection and no connection, respectively.

(Figures 4I–4K and S4). Moreover, all neuronal components of the entorhinal L1 SBC-led disinhibitory circuit were confined within columnar areas with a radius of ~75 µm beneath the SBCs (Figures 4K–4L and S4). These results indicate that entorhinal L1 SBC-led disinhibitory circuits exhibit the translaminar, unidirectional, and minicolumnar disinhibition features identical to those in the neocortex. The findings support the idea that the modular organizational architecture is applicable across all cortical areas.

Reconstructing sufficient elements, including both neurons and their connections, of L1 SBC-led disinhibitory circuits across somatosensory, motor, prefrontal, and entorhinal cortical areas yields several generalized architectural features (Figures 4M–4Q). First, L1 SBCs inhibit at least ~30% interneurons and

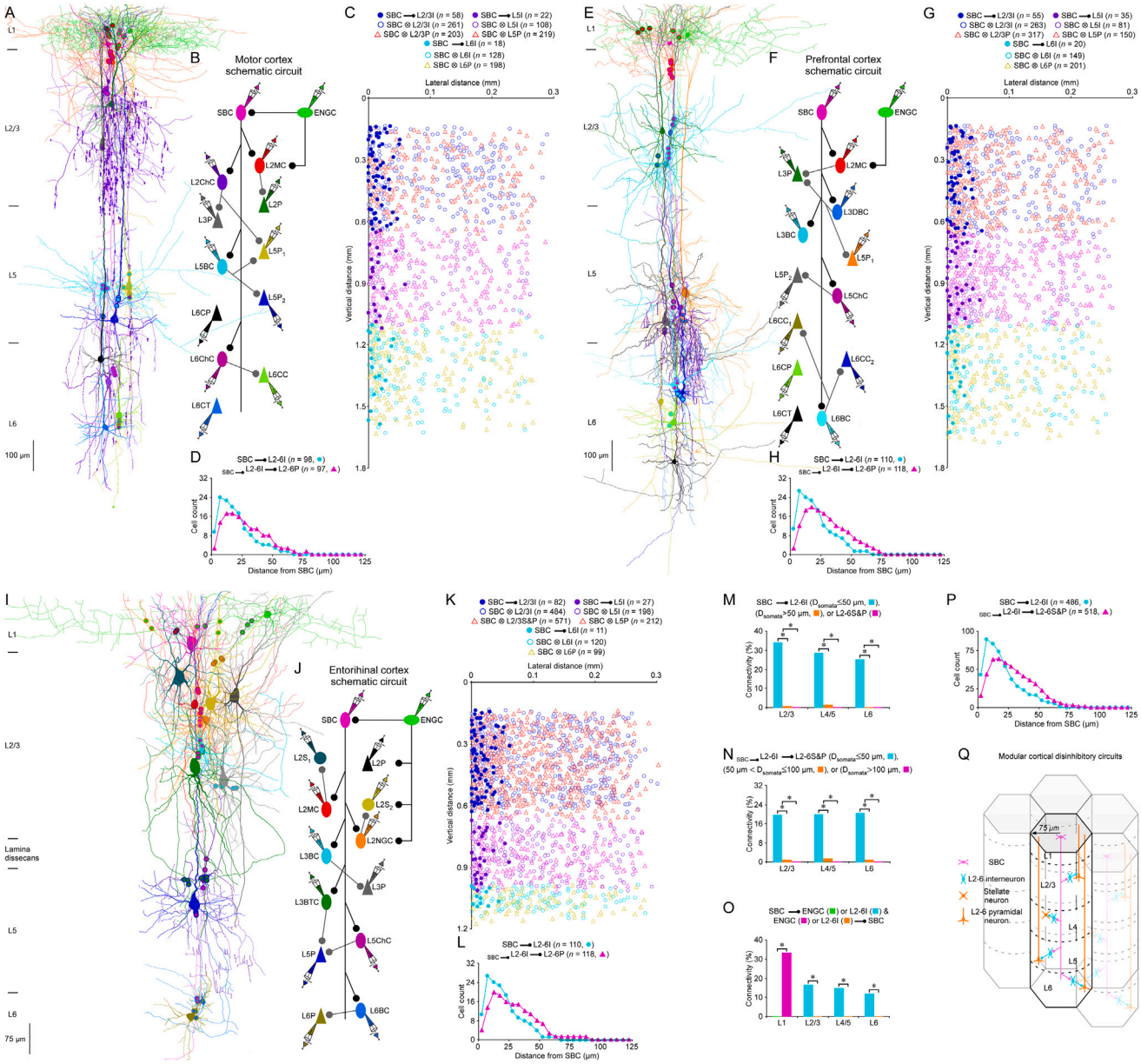

Figure 4. L1 SBCs lead modular disinhibitory circuits in the cortex

(A) Reconstruction of L1 SBC (pink), ENGC (green), and multiple L2-6 interneurons and pyramidal neurons recorded simultaneously from a mouse acute motor cortical slice. The double colored dots indicate putative synaptic contacts.

(B) The schematic shows synaptic connections.

(C) The plot shows relative distances from L2-6 interneurons and pyramidal neurons to SBCs (horizontal distance in the x axis) and the cortical pia surface (vertical distance in the y axis).

(D) Lateral distributions of SBC-inhibited L2-6 interneurons and SBC-disinhibited L2-6 pyramidal neurons in the motor cortex. See also Figure S1.

(E) Reconstruction of L1 SBC (pink), ENGC (green), and multiple L2-6 interneurons and pyramidal neurons recorded simultaneously from a mouse acute prefrontal cortical slice. The double colored dots indicate putative synaptic contacts.

(F) The schematic shows synaptic connections.

(G) The plot shows relative distances from L2-6 interneurons and pyramidal neurons to SBCs (horizontal distance in the x axis) and the cortical pia surface (vertical distance in the y axis).

(H) Lateral distributions of SBC-inhibited L2-6 interneurons and SBC-disinhibited L2-6 pyramidal neurons of the prefrontal cortex. See also Figure S2.

(I) Reconstruction of L1 SBC (pink), ENGC (green), and multiple L2-6 interneurons, stellate, and pyramidal neurons recorded simultaneously from a mouse acute medial entorhinal cortical slice. The double colored dots indicate putative synaptic contacts.

(J) The schematic shows synaptic connections.

(legend continued on next page)

disinhibit at least ~20% stellate and pyramidal neurons in L2-6 in the cortex (Figures 4M–4N), resulting in the translaminar disinhibition on excitatory neurons. Second, L1 SBCs exhibit 100% unidirectional inhibition on L2-6 interneurons, enabling disinhibition of L2-6 stellate and pyramidal neurons in the cortex (Figure 4O), effectively controlling the output of local pools of cortical excitatory neurons. Third, L1 SBCs inhibit L2-6 interneurons and disinhibit L2-6 stellate and pyramidal neurons within narrow columns of ~75 μm in radius in the cortex, establishing the spatially restricted minicolumnar-like disinhibition (Figure 4P). Finally, L1 SBCs form disinhibitory circuits without sharing neuronal constituents, creating the functionally independent disinhibition (Figure 4Q).

Specific deficits at SBC-disinhibited synapses in Alzheimer's brains

A long-standing hypothesis postulates that minor impairments confined to specific circuits or synapses within modular circuits can disproportionately disrupt the neural function, potentially leading to severe neurological disorders.[44] The role of specific interneuronal dysfunction in the pathogenesis of Alzheimer's disease remains controversial.[45–47] Given the essential role of L1 SBC-led disinhibition in Alzheimer's-related high cognitive functions,[48,49] we investigated architectural organization of disinhibitory circuits in the medial entorhinal cortex of senescence-accelerated mouse prone 8 (SAMP8), a spontaneous accelerated aging mouse line.[50] SAMP8 mice are considered as a robust model of sporadic Alzheimer's disease because these mice harbor the Alzheimer's-like neuropathological phenotypes, β-amyloid deposits, Tau-like neurofibrillary tangles, and behavioral alterations most closely representing the Alzheimer's complexity.[51] Octuple-sexdecuple patch-clamp recordings demonstrated that entorhinal L1 SBCs led translaminar, unidirectional, and minicolumnar disinhibitory circuits in 2- and 10-month-old SAMP8 mice (Figures 5A–5D, S5, and S6). Quantitative analysis showed that while SAMP8 mice had the same inhibitory connection from SBCs to L2-6 interneurons as wild-type (WT) mice, there was a progressive reduction in inhibitory connectivity from SBC-inhibited L2-6 interneurons to L2-6 stellate and pyramidal neurons with aging (Figure 5E). These results suggest age-dependent specific deficits at synapses disinhibited by SBCs.

As controls, we analyzed L1 ENGC-led inhibitory circuits, which regulate and assist L1 SBC-led disinhibitory circuits in salient selection.[5,6,52] No difference was detected in the inhibitory connection from ENGCs to SBCs of WT and SAMP8 mice at different ages, indicating that L1 SBC-led disinhibitory circuits receive the same inhibitory regulation from ENGCs (Figure 5F). Moreover, there was no difference in the inhibitory connection between ENGCs and L2/3 interneurons, between ENGCs and L2-6 pyramidal neurons, and between ENGC-inhibited L2/3 interneurons and L2-6 pyramidal neurons in both WT and SAMP8 mice of various ages (Figure 5G). These results suggest that there were no deficits in L1 ENGC-led inhibitory circuits, including no deficits at inhibitory synapses formed by ENGC-inhibited L2/3 interneurons on L2-6 pyramidal neurons. Together, these results suggest that SAMP8 mice develop age-dependent, circuit- and connection-specific deficits within L1 SBC-led disinhibitory minicolumnar circuits, implying their potential relevance to Alzheimer's disease pathology.

We then extended our analysis to other cortical areas in SAMP8 mice to examine the specific deficits at SBC-disinhibited synapses. Octuple-sexdecuple patch-clamp recordings revealed a sequential development of age-dependent specific deficits in L1 SBC-led disinhibitory minicolumnar circuits across different cortical areas in SAMP8 mice. The deficits initially emerged in the medial entorhinal cortex during the first 2 postnatal months, followed by the prefrontal cortex (at 4–6 months) and sensorimotor cortices (at 8–10 months) (Figures 5E and 6F). These deficits progressively worsened with age (Figures 5E and 6F). These results indicate a pattern of sequential development and spread of age-dependent specific deficits in L1 SBC-led disinhibitory minicolumnar circuits, reminiscent of the progressive spread of pathology observed in Alzheimer's disease.

The spread of deficits of SBC-disinhibited synapses from the medial entorhinal cortex to the prefrontal and other cortical areas appears to correlate with the development of Alzheimer's cognitive impairments early in spatial navigation, learning, and memory, and later in complex attentional, executive, and other functions.[53,54] Hence, we used fear conditioning and Morris water

(K) The plot of relative distances from L2-6 interneurons, stellate, and pyramidal neurons to SBCs (horizontal distance in the x axis) and the cortical pia surface (vertical distance in the y axis). Note in (C), (G), and (K), filled and empty dots (interneurons) or triangles (pyramidal neurons) represent connected and unconnected neurons, respectively.

(L) Lateral distributions of SBC-inhibited L2-6 interneurons and SBC-disinhibited L2-6 stellate and pyramidal neurons in the medial entorhinal cortex. See also Figure S4.

(M) Average values for the connectivity between SBCs and L2-6 interneurons, stellate, or pyramidal neurons in the somatosensory, motor, prefrontal, and medial entorhinal cortices.

(N) Average values for the connectivity between SBC-inhibited L2-6 interneurons and L2-6 stellate or pyramidal neurons in the somatosensory, motor, prefrontal, and medial entorhinal cortices.

(O) Average values for the connectivity between SBCs and ENGCs or L2-6 interneurons in the somatosensory, motor, prefrontal, and medial entorhinal cortices. Asterisks in (M)–(O) indicate $p < 0.05$ (chi-squared tests).

(P) Lateral distribution of SBC-inhibited L2-6 interneurons and SBC-disinhibited L2-6 stellate or pyramidal neurons in the somatosensory, motor, prefrontal, and medial entorhinal cortices.

Note —● and ⊗ in (C), (D), (G), (H), (K), (L), and (M)–(P) represent synaptic connection and no connection, respectively.

(Q) Model for modular cortical translaminar, unidirectional, minicolumnar, and independent disinhibitory circuits. Note the minicolumnar architecture enclosing an area of ~75 μm in radius, enough to accommodate roughly a set of dendritic bundle (~30–60 μm in dimeter), a set of axonal bundle (~15–30 μm in dimeter), and the associated L2-6 neurons at any of its radial direction (and up to ~6–8 sets in all directions) or ~1,500 neurons.[38,39]

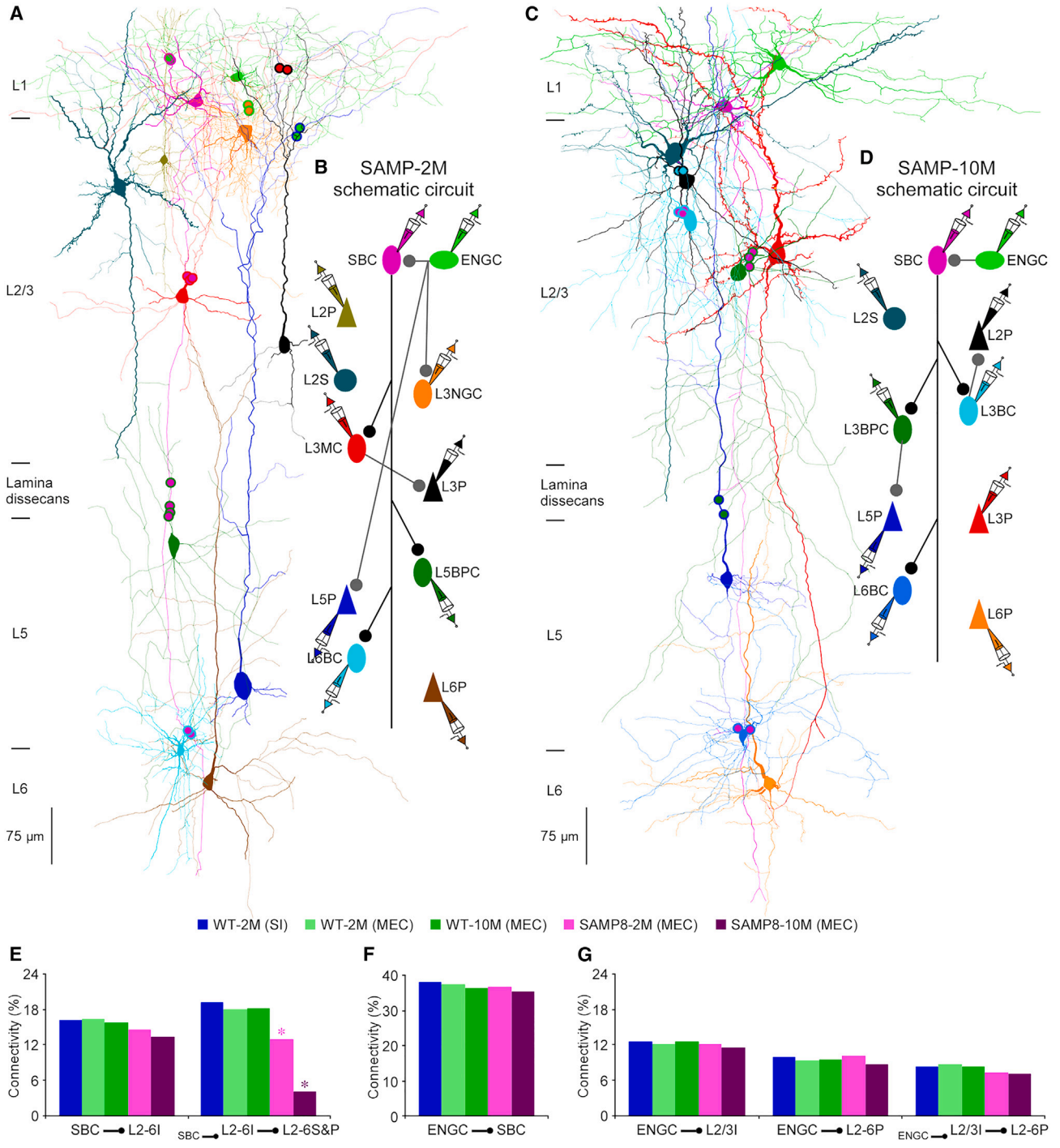

Figure 5. Selective deficits in L1 SBC-led modular disinhibitory circuits in SAMP8 mice

(A) Reconstruction of L1 SBC (pink), ENGC (green), and multiple L2-6 interneurons, stellate, and pyramidal neurons recorded simultaneously from an acute medial entorhinal cortical slice of A 2-month-old SAMP8 mouse. The double colored dots indicate putative synaptic contacts.

(B) The schematic shows synaptic connections.

(C) Reconstruction of L1 SBC (pink), ENGC (green), and multiple L2-6 interneurons, stellate, and pyramidal neurons recorded simultaneously from an acute medial entorhinal cortical slice of A 10-month-old SAMP8 mouse. The double colored dots indicate putative synaptic contacts.

(D) The schematic shows synaptic connections.

(E) Values for the connectivity between SBCs and L2-6 interneurons (WT-2M [SI]: 16.09%, n = 348; WT-2M [MEC]: 16.36%, n = 55, χ^2 = 0.0026, p = 0.959; WT-10M (MEC): 15.71%, n = 70, χ^2 = 0.0062, p = 0.937; SAMP8-2M [MEC]: 14.49%, n = 207, χ^2 = 0.2535, p = 0.615; SAMP8-10M [MEC]: 13.33%, n = 120, χ^2 =

(legend continued on next page)

maze hidden-platform tests to evaluate the cognitive function of WT and SAMP8 mice. During fear conditioning, both SAMP8 and WT mice displayed similar responses to the tone and footshock, as well as comparable levels of freezing during the training phase (Figures 6A and 6B). However, during the memory testing conducted 24 h after fear conditioning, SAMP8 mice exhibited a gradual reduction in freezing behavior compared with WT mice as they aged (Figure 6B), indicative of an age-dependent impairment in associative memory.

To verify the findings, we conducted the Morris water maze hidden-platform tests. Over the course of the training period, WT mice displayed a significant decrease in the latency required to find the hidden platform, indicating improved spatial learning, whereas SAMP8 mice consistently showed longer escape latencies with less improvement (Figures 6C and 6D). During the probe trial on day 7, when the platform was removed from the swimming pool, WT mice spent more time in the target quadrant where the platform had previously been placed, whereas SAMP8 mice spent relatively more similar amounts of time in all four quadrants (Figure 6E), indicating an impairment in spatial memory. Older SMAP8 mice exhibited more pronounced impairments in spatial learning and memory (Figure 6E). Importantly, the severity of specific deficits at SBC-disinhibited synapses in cortical minicolumnar circuits showed a linear correlation with the degree of learning and memory impairments in SAMP8 mice as they age (Figures 6F–6H). This correlation supports the notion that the circuit- and connection-specific deficits at SBC-disinhibited synapses are closely associated with Alzheimer's-like cognitive impairments in SAMP8 mice. Taken together, the observed age dependence, spread of cortical pathology, and correlation with cognitive impairments indicate that the circuit- and connection-specific deficits at SBC-disinhibited synapses in cortical minicolumnar circuits are closely correlated with Alzheimer's-like cognitive impairments in SAMP8 mice.

DISCUSSION

This study reports the development of a simultaneous and sequential octuple-sexdecuple whole-cell patch-clamp recording system that enables interconnection analysis of a large number of neurons and multiple associated circuit motifs to achieve architectural reconstruction of complex cortical circuits. Architectural reconstruction of L1 SBC-led disinhibitory neuronal circuits in the mouse somatosensory, motor, prefrontal, and medial entorhinal cortical areas unveils a modular cortical elementary processing circuit. The modular cortical circuit features the translaminar, unidirectional, minicolumnar, and independent disinhibition (Figure 4Q). Moreover, architectural reconstruction of L1 SBC-led disinhibitory minicolumnar circuits in senescence-accelerated mouse prone 8 validates the modular cortical circuit architecture and discloses the specific deficits at SBC-disinhibited synapses in this Alzheimer's mouse model. The circuit- and connection-specific deficits exhibit properties characteristic Alzheimer's disease, suggesting a disinhibition mechanism associated with this condition. These results validate the applicability of octuple-sexdecuple patch-clamp recordings in deciphering complex cortical circuits in healthy and diseased brains.

Architectural reconstruction of complex circuits

The central tenet of connectomics is to reconstruct sufficient neuronal constituents with their synaptic connections of a neural circuit to reveal its architectural organization that dictates basic principles of brain operation.[1,2,13] However, existing techniques struggle in interconnection analysis of a large number of neurons and multiple circuit motifs to reconstruct architectural schemes of complex cortical circuits, even though they are effective in illuminating the fine details of cortical circuit motifs.[14–16] This report shows that octuple-sexdecuple patch-clamp recordings enable interconnection analysis among a large number of neurons and associated circuit motifs in complex cortical circuits. The analysis yields the architectural structure of a cortical complex circuit—the modular L1 SBC-led disinhibitory minicolumnar circuit. The architectural scheme reveals that individual L1 SBCs connect multiple disinhibitory circuit motifs mediated by distinct types of interneurons (i.e., L2-6 MCs, NGCs, BTCs, BPCs, BCs, DBCs, and ChCs) and excitatory neurons (i.e., L2-6 stellate and pyramidal neurons). The disinhibitory circuit motifs are parallelly linked, forming complex circuits that achieve translaminar, unidirectional, minicolumnar, and independent disinhibition. The findings validate the capable of octuple-sexdecuple patch-clamp recordings in elucidating architectures of complex cortical circuits. The knowledge, which bridges the gap between the properties of cortical neurons or circuit motifs and the operation of the cortex, contributes to a better understanding of the neural basis of behavior. Moreover, the discovery of cortical architectural designs holds promise for advancements in artificial intelligence.[2] The rudimentary knowledge of cortical circuit organization and operational design has already inspired the

0.5216, p = 0.470) and between SBC-inhibited L2-6 interneurons and L2-6 stellate or pyramidal neurons (WT-2M [SI]: 19.10%, n = 377; WT-2M [MEC]: 18.00%, n = 50, χ^2 = 0.0346, p = 0.852; WT-10M [MEC]: 18.07%, n = 83, χ^2 = 0.0467, p = 0.829; SAMP8-2M [MEC]: 12.83%, n = 226, χ^2 = 3.9788, p = 0.046; SAMP8-10M [MEC]: 3.97%, n = 126, χ^2 = 16.6744, p < 0.0005).
(F) Values for the connectivity between ENGCs and SBCs (WT-2M [SI]: 37.50%, n = 16; WT-2M [MEC]: 36.84%, n = 19, χ^2 = 0.0016, p = 0.968; WT-10M [MEC]: 36.00%, n = 25, χ^2 = 0.0095, p = 0.923; SAMP8-2M [MEC]: 36.36%, n = 22, χ^2 = 0.0051, p = 0.943; SAMP8-10M [MEC]: 35.00%, n = 20, χ^2 = 0.0241, p = 0.877).
(G) Values for the connectivity between ENGCs and L2/3 interneurons (WT-2M [SI]: 20.73%, n = 632; WT-2M [MEC]: 20.24%, n = 588, χ^2 = 0.0448, p = 0.832; WT-10M [MEC]: 20.97%, n = 434, χ^2 = 0.0090, p = 0.925; SAMP8-2M [MEC]: 20.15%, n = 402, χ^2 = 0.0505, p = 0.822; SAMP8-10M [MEC]: 19.00%, n = 379, χ^2 = 0.4421, p = 0.506), between ENGCs and L2-6 pyramidal neurons (WT-2M [SI]: 16.40%, n = 372; WT-2M [MEC]: 15.54%, n = 354, χ^2 = 0.1002, p = 0.752; WT-10M [MEC]: 15.66%, n = 249, χ^2 = 0.0597, p = 0.807; SAMP8-2M [MEC]: 16.67%, n = 306, χ^2 = 0.0088, p = 0.925; SAMP8-10M [MEC]: 14.50%, n = 274, χ^2 = 0.3873, p = 0.534), and between ENGC-inhibited L2/3 interneurons and L2-6 pyramidal neurons (WT-2M [SI]: 13.79%, n = 319; WT-2M [MEC]: 14.44%, n = 187, χ^2 = 0.0407, p = 0.840; WT-10M [MEC]: 13.62%, n = 257, χ^2 = 0.0037, p = 0.952; SAMP8-2M [MEC]: 12.09%, n = 215, χ^2 = 0.3259, p = 0.568; SAMP8-10M [MEC]: 11.388, n = 202, χ^2 = 0.3984, p = 0.528) in the somatosensory cortex of 2-month-old wild-type mice, medial entorhinal cortex of 2-month and 10-month-old wild-type mice, and medial entorhinal cortex of 2-month and 10-month-old SAMP8 mice. Asterisks indicate p < 0.05 (chi-squared tests).

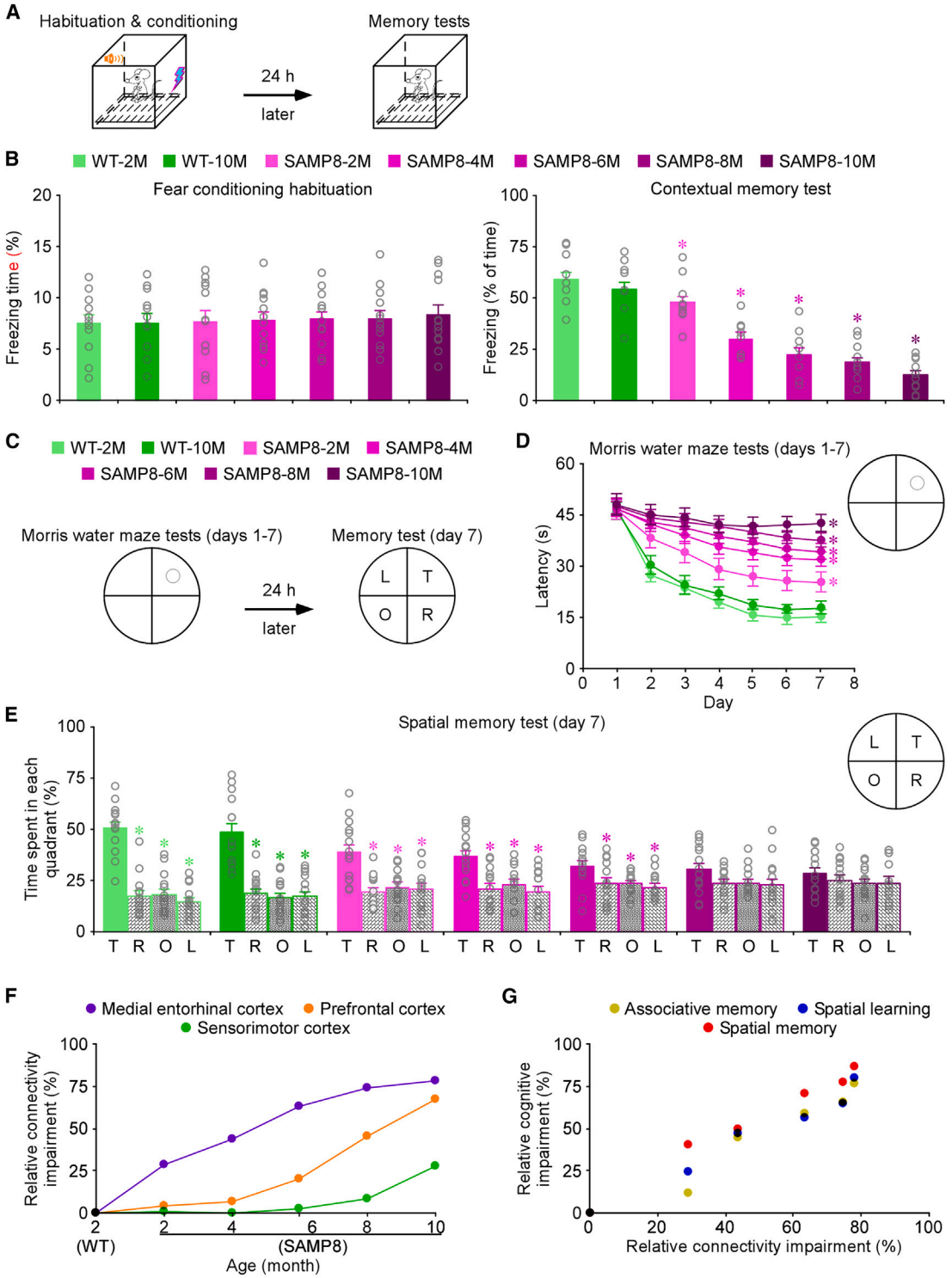

Figure 6. Selective deficits in L1 SBC-led modular disinhibitory circuits in SAMP8 mice

(A) The schematic shows associative learning test.

(B) Left, freezing time of 10-month-old wild-type mice (7.55% ± 0.88%, n = 12, $U = 73.0$, p = 0.979), and 2-month-old (7.67% ± 1.08%, n = 12, $U = 75.5$, p = 0.862), 4-month-old (7.77% ± 0.82%, n = 12, $U = 73.0$, p = 0.977), 6-month-old (7.90% ± 0.77%, n = 12, $U = 77.0$, p = 0.795), 8-month-old (7.96% ± 0.84%, n = 12, $U = 75.0$, p = 0.885), and 10-month-old (8.28% ± 1.00%, n = 12, $U = 75.5$, p = 0.862) SAMP8 mice compared with control 2-month-old wild-type mice (7.44% ± 0.84%, n = 12) during conditioning. Right, freezing time of 10-month-old wild-type mice (54.11% ± 3.82%, n = 12, $U = 57.0$, p = 0.403), and 2-month-old (47.87% ±

(legend continued on next page)

development of convolutional neural networks (CNNs) and CNN-based machine learning.[55,56] Similarly, the insights gained from the intricate architectural design of cortical minicolumns may further revolutionize artificial neural networks.

Disinhibitory circuits

The reported disinhibitory circuit motifs, led by either VIP-expressing neurons or L1 SBCs, appear to be conserved across various cortical areas.[5,6,12,14,33,57–61] However, it is important to note that VIP-expressing neurons exhibit heterogeneity in their constituent cell types, which can contribute to differences in the specific circuit motifs they form. In many cases, VIP cells form mutual inhibitory connections with other interneurons,[14,32,59] although there are exceptions.[14] Additionally, some VIP cells are known to directly inhibit excitatory neurons.[33] Finally, the relationship between L1 SBCs and VIP cells is still not fully understood, and it remains uncertain whether L1 SBCs belong to a subset of VIP cells.[25] This indicates that further investigation is necessary to determine whether all VIP cells or only a specific subset of them are involved in achieving disinhibition and the mechanisms by which disinhibition is achieved.

This study provides new insights into the mechanism by which L1 SBC-led disinhibitory circuits achieve salient selection. Salient selection is a process that develops postnatally and relies on dendritic calcium spikes,[62,63] which is also postnatally developed and functions as a coincidence detection mechanism governing the output of excitatory neurons.[62,64,65] L1 SBC-led disinhibitory circuits relieve a small number of excitatory neurons from the powerful, widespread inhibition mediated by L1 ENGC-led inhibitory circuits. By doing so, the disinhibitory circuits enable this small number of excitatory neurons to carry out coincidence detection of salient information.[5,6] In turn, L1 ENGC-led inhibitory circuits terminate the disinhibition and coincidence detection by inhibiting L1 SBCs.[5,52] Thus, SBC-led disinhibitory circuits and ENGC-led inhibitory circuits work as a consummate team to effectively filter out "noise" in the incoming information and enhance attention to salient signals. In this study, the new data show that L1 SBCs selectively inhibit interneurons in the deeper cortical layers (from L2 to L6) in a unidirectional manner, without inhibiting any stellate or pyramidal neurons within the layers. This finding confirms the dominant control exerted by SBCs over excitatory neurons. Further architectural analysis reveals that L1 SBCs establish translaminar, unidirectional, minicolumnar, and independent disinhibitory circuits that are conserved across different cortical areas. This modular design supports a model that the same salient selection circuitry is employed to achieve diverse information processing in various cortical areas. Furthermore, it provides an explanation for the involvement of L1 SBC-led disinhibitory circuits in varied higher cognitive functions such as perception, attention, spatial navigation, learning, and memory.[7–12,42] In summary, the study sheds light on how L1 SBC-led disinhibitory circuits contribute to salient selection in cortical circuits. The modular circuitry observed suggests a common mechanism for achieving salient selection across different cortical areas, providing insights into the role of these circuits in various cognitive behaviors.

Cortical modular minicolumnar circuits

The minicolumnar-like parcellation of the cortex has been a prominent model for understanding cortical function and the subject of debate since its introduction in 1957.[66,67] Based on a collection of anatomical, physiological, and metabolism activity work that supports the existence of cortical periodicity, Mountcastle and others brought together a bold minicolumnar hypothesis. The Mountcastle model postulates that a tightly knitted local pool of neurons in cortical minicolumns form a concentrated circuitry that serves as the cortical elementary processing unit of cortex.[36] Recent studies have identified a few circuit motifs that could potentially function as components of minicolumnar circuits.[59,60,68] However, due to the technical challenges involved in revealing the overall structure of canonical neuronal circuits within cortical minicolumns, the legitimacy of the minicolumnar theory remains unverified. As a result, our understanding of whether modular minicolumnar circuits exist in the cortex and, if they do, how they are designed to operate and accomplish complex behaviors remains limited.[34,35,38,69]

2.92%, n = 12, $U = 36.0$, p = 0.040), 4-month-old (30.02% ± 3.26%, n = 12, $U = 6.0$, $p < 0.001$), 6-month-old (22.26% ± 3.37%, n = 12, $U = 3.0$, $p < 0.001$), 8-month-old (18.72% ± 2.33%, n = 12, $U = 0.0$, $p < 0.001$), and 10-month-old (12.78% ± 2.11%, n = 12, $U = 0.0$, $p < 0.001$) SAMP8 mice compared with control 2-month-old wild-type mice (59.32% ± 3.92%, n = 12) in contextual learning tests.

(C) The schematic shows MWM spatial learning test.

(D) Escape latency of 10-month-old wild-type mice (23.1 ± 1.7 s, n = 14, $U = 134.5$, p = 0.098), and 2-month-old (30.3 ± 2.8 s, n = 14, $U = 163.0$, p = 0.003), 4-month-old (37.1 ± 2.2 s, n = 14, $U = 184.0$, $p < 0.001$), 6-month-old (39.8 ± 2.4 s, n = 14, $U = 185.5$, $p < 0.001$), 8-month-old (42.9 ± 2.0 s, n = 14, $U = 194.0$, $p < 0.001$), and 10-month-old (47.9 ± 2.3 s, n = 14, $U = 196.0$, $p < 0.001$) SAMP8 mice compared with control 2-month-old wild-type mice (20.3 ± 1.8 s, n = 14) during Morris water maze tests on day 7.

(E) Relative swimming time in each quadrant of 2-month-old (T: 50.2% ± 3.2%, R: 17.1% ± 2.6%, O: 18.0% ± 2.6%, L: 14.7% ± 1.9%, n = 14, $3.0 \leq U \leq 5.0$, $p < 0.001$) and 10-month-old (T: 48.2% ± 4.5%, R: 18.6% ± 2.3%, O: 16.2% ± 2.3%, L: 17.0% ± 2.6%, n = 14, $4.0 \leq U \leq 5.0$, $p < 0.001$) wild-type mice and of 2-month-old (T: 38.9% ± 3.9%, R: 19.1% ± 2.1%, O: 21.6% ± 2.2%, L: 24.6% ± 2.8%, n = 14, $21.0 \leq U \leq 23.0$, $p \leq 0.002$), 4-month-old (T: 36.6% ± 3.0%, R: 21.0% ± 2.5%, O: 23.0% ± 2.2%, L: 19.3% ± 3.0%, n = 14, $27.0 \leq U \leq 32.5$, $p < 0.003$), 6-month-old (T: 31.7% ± 2.7%, R: 23.2% ± 2.7%, O: 23.4% ± 1.4%, L: 21.7% ± 1.7%, n = 14, $34.0 \leq U \leq 57.0$, $0.004 \leq p \leq 0.063$), 8-month-old (T: 30.2% ± 3.1%, R: 23.5% ± 1.9%, O: 23.8% ± 1.8%, L: 22.5% ± 3.2%, n = 14, $61.0 \leq U \leq 69.0$, $p > 0.05$), and 10-month-old (T: 28.2% ± 2.7%, R: 24.8% ± 2.5%, O: 23.4% ± 2.1%, L: 23.6% ± 3.3%, n = 14, $71.5 \leq U \leq 77.0$, $p > 0.250$) SAMP8 mice in probe trials on day 7. Data are represented as mean ± SEM in (B), (D), and (E). Asterisks indicate $p < 0.05$ (Mann-Whitney Rank Sum tests).

(F) The plot shows progressive deficits in inhibitory connection between SBC-inhibited L2-6 interneurons and stellate or pyramidal neurons in the medial entorhinal, prefrontal, and sensorimotor cortices of SAMP8 mice at different ages.

(G) The plot shows correlations between cognitive impairments, including associative memory (n = 6; normality test passed, p = 0.67; constant variance test passed, p = 0.06; $r = 0.974$, $F = 75.0$, $p < 0.001$), spatial learning (n = 6; normality test passed, p = 0.75; constant variance test passed, p = 0.06; $r = 0.985$, $F = 128.5$, $p < 0.001$), or spatial memory (n = 6; normality test passed, p = 0.16; constant variance passed, p = 0.06; $r = 0.993$, $F = 208.4$, $p < 0.001$), and specific deficits at SBC-disinhibited synapses in the medial entorhinal cortex of SAMP8 mice at different ages.

The architectural reconstruction of L1 SBC-led modular disinhibitory circuits provides valuable insights into the design and operational principles of cortical minicolumnar circuits. One key aspect addressed by the reconstruction is the involvement of L1 neurons in the formation and operation of minicolumns, which is unanswered in the minicolumnar model due to lack of experimental data.[36] The reconstruction here shows that L1 SBCs epicentrally lead the translaminar canonical disinhibitory circuits, underscoring the vital role of cortical L1 neurons and the participation of neurons across all cortical layers. The translaminar architectural design permits the canonical circuits to utilize and coordinate inputs and outputs from all layers, adding complexity to cortical processing.

Another important architectural feature revealed by the reconstruction is that L1 SBCs form unidirectional inhibition on L2-6 interneurons, and execute unidirectional disinhibition on L2-6 stellate and pyramidal neurons. The dominative architectural design allows L1 SBCs to diminish the autonomy of other neurons in canonical circuits and dominate the output of minicolumns. Such cooperation among a large number of neurons within minicolumns facilitates the attainment of subtlety and plasticity in cortical processing.

The reconstructed L1 SBC-led disinhibitory circuits span an area of ~75 μm in radius (Figure 4Q). This size is sufficient to accommodate dendritic (~30–60 μm in dimeter) and axonal bundle (~15–30 μm in dimeter) as well as associated L2-6 neurons in ~6–8 radial directions. Assuming the number of neurons involved in single sets of dendritic and axonal bundles being ~180 (cf. Jones[38]), the estimated number of neurons housed in single cortical minicolumns is ~1,260. This estimation closely matches the estimated ~1,660 neurons per minicolumnar area based on cortical neuron density (cf. Carlo and Stevens[39]). Considering the standard sizing of cortical columns as slightly elongated hexagons with a diameter of ~300–400 μm in diameter,[36] this information suggests that each cortical column consists of ~7 minicolumns arranged in presumably hexagonal structures (Figure 4Q). The average distance of pair-recorded SBCs is ~140 μm (Figure 3). This suggests that individual minicolumnar disinhibitory circuits are likely led by single SBCs. Finally, the reconstruction answers another unresolved issue of whether minicolumnar circuits function independently. Simultaneous recordings show that SBC-led disinhibitory circuits do not intermingle, indicating independent operation between minicolumns. The minicolumnar and independent architectural schemes enhance variation and redundancy in cortical processing.

Overall, the architectural analysis of the elementary processing circuit within cortical minicolumns provides new insights into operational principles of the cortex. Within cortical minicolumns, 1,500-neuron canonical circuits, which harness the power of local pools of large numbers of cortical neurons, serve as basic functional units for complex tasks with precision and plasticity. This high-density local neuronal connectivity design is advantageous in terms of physical organization and efficiency. Between cortical minicolumns and cortical areas, the cortex utilizes multiplied canonical circuits in parallel to effectively handle diverse tasks and maintain resilience to the loss of a large cortical area, such as in hemispherectomy, due to redundancy.

Clinical implication

The advantageous architectural design of L1 SBC-led modular disinhibitory circuits may make them susceptible to relatively minor impairments that could disrupt cortical operation in a disproportionate manner.[44] Inspired by this possibility, we examined the architectural organization of L1 SBC-led disinhibitory circuits in an Alzheimer's mouse model. The analysis discloses relatively minor, circuit- and connection-specific deficits in minicolumnar disinhibitory circuits, which take place at SBC-disinhibited synapses made by SBC-inhibited L2-6 interneurons on L2-6 stellate and pyramidal neurons, but not at SBC-inhibited synapses. On the other hand, in L1 ENGC-led inhibitory circuits, no deficits are observed at inhibitory synapses made by ENGCs on SBCs, on L2/3 interneurons, and L2-6 pyramidal neurons, as well as those made by ENGC-inhibited L2/3 interneurons on L2-6 pyramidal neurons. Quantitative analysis shows that the specific deficits at SBC-disinhibited synapses exhibit characteristic Alzheimer's-like age-dependent patterns, cortical spread, and correlation with cognitive impairments (Figures 6F and 6G), suggesting a disinhibition-mediated mechanism that may contribute to the development of Alzheimer's disease.

The specific deficits at SBC-disinhibited synapses, but not other inhibitory synapses, account for the disinhibition seen in Alzheimer's brains and help to explain many conflicting effects of global inhibitory manipulations on cognitive impairments associated with the disease.[45–47] Similar disinhibition-like synaptic pathology is observed in the other two widely used Alzheimer's mouse models, ApoE4 and Tau(P301S) transgenic mice.[46,70–72] It would be intriguing in the future to investigate whether specific deficits at SBC-disinhibited synapses represent a generalized, converging pathogenic mechanism at the neuronal circuit level for multiple genetic forms of Alzheimer's disease.

Furthermore, minor alterations in modular cortical circuits could contribute to other disorders, such as autism, schizophrenia, depression, and epilepsy.[44] The use of octuple-sexdecuple patch-clamp recordings allows quantitative analysis of complex cortical circuit architectures, facilitating the effort of causally linking complex cortical circuit properties with physiological actions, clinical symptoms in diseases, and therapeutic benefits.

Limitations of the study

Despite the integration of automatic procedures, octuple-sexdecuple patch-clamp recordings still require manual operation for the delicate gigasealing step, making it still a skill-demanding approach. This is due in part to the need for a high-quality seal between the recording electrode and the target neuron's membrane, which is essential for rigorous connectivity analysis. Regarding the specific deficits identified at SBC-disinhibited synapses, further experiments are necessary to determine the precise nature of these deficits. It is important to investigate whether the disinhibitory deficits are specific to certain presynaptic interneuron types (such as MCs, NGCs, BTCs, BPCs, BCs, DBCs, and/or ChCs), specific postsynaptic excitatory neuron populations, and/or specific cortical layers.

STAR★METHODS

Detailed methods are provided in the online version of this paper and include the following:

- KEY RESOURCES TABLE
- RESOURCE AVAILABILITY
  - Lead contact
  - Materials availability
  - Data and code availability
- EXPERIMENTAL MODEL AND SUBJECT PARTICIPANT DETAILS
- METHOD DETAILS
  - Parallel brain slice preparation
  - Electrophysiology
  - Octuple-sexdecuple recording system
  - Morphology reconstruction
  - Behavioral analysis
- QUANTIFICATION AND STATISTICAL ANALYSIS
  - Statistical analysis

SUPPLEMENTAL INFORMATION

Supplemental information can be found online at https://doi.org/10.1016/j.celrep.2023.112904.

ACKNOWLEDGMENTS

I thank Drs. Menno Witter, May-Britt Moser, and Edvard Moser for their inspiring discussions, and members of the Zhu laboratory for comments and technical assistance. This sabbatical work is supported in part by NIH. J.J.Z. holds the Radboud Excellence Professorship.

AUTHOR CONTRIBUTIONS

J.J.Z. conceived the concept, carried out the experiments, analyzed the data, and wrote the manuscript.

DECLARATION OF INTERESTS

The author declares no competing interests.

Received: February 15, 2023
Revised: June 21, 2023
Accepted: July 13, 2023
Published: July 31, 2023

REFERENCES

1. Abbott, L.F., Bock, D.D., Callaway, E.M., Denk, W., Dulac, C., Fairhall, A.L., Fiete, I., Harris, K.M., Helmstaedter, M., Jain, V., et al. (2020). The mind of a mouse. Cell *182*, 1372–1376. https://doi.org/10.1016/j.cell.2020.08.010.
2. Luo, L. (2021). Architectures of neuronal circuits. Science *373*, eabg7285. https://doi.org/10.1126/science.abg7285.
3. Kim, C.K., Adhikari, A., and Deisseroth, K. (2017). Integration of optogenetics with complementary methodologies in systems neuroscience. Nat. Rev. Neurosci. *18*, 222–235. https://doi.org/10.1038/nrn.2017.15.
4. Luo, L., Callaway, E.M., and Svoboda, K. (2018). Genetic dissection of neural circuits: a decade of progress. Neuron *98*, 256–281. https://doi.org/10.1016/j.neuron.2018.03.040.
5. Jiang, X., Wang, G., Lee, A.J., Stornetta, R.L., and Zhu, J.J. (2013). The organization of two new cortical interneuronal circuits. Nat. Neurosci. *16*, 210–218. https://doi.org/10.1038/nn.3305.
6. Lee, A.J., Wang, G., Jiang, X., Johnson, S.M., Hoang, E.T., Lanté, F., Stornetta, R.L., Beenhakker, M.P., Shen, Y., and Julius Zhu, J. (2015). Canonical organization of layer 1 neuron-led cortical inhibitory and disinhibitory interneuronal circuits. Cerebr. Cortex *25*, 2114–2126. https://doi.org/10.1093/cercor/bhu020.
7. Cichon, J., and Gan, W.B. (2015). Branch-specific dendritic Ca^{2+} spikes cause persistent synaptic plasticity. Nature *520*, 180–185. https://doi.org/10.1038/nature14251.
8. Takahashi, N., Oertner, T.G., Hegemann, P., and Larkum, M.E. (2016). Active cortical dendrites modulate perception. Science *354*, 1587–1590. https://doi.org/10.1126/science.aah6066.
9. Doron, G., Shin, J.N., Takahashi, N., Drüke, M., Bocklisch, C., Skenderi, S., de Mont, L., Toumazou, M., Ledderose, J., Brecht, M., et al. (2020). Perirhinal input to neocortical layer 1 controls learning. Science *370*, eaaz3136. https://doi.org/10.1126/science.aaz3136.
10. Pardi, M.B., Vogenstahl, J., Dalmay, T., Spanò, T., Pu, D.L., Naumann, L.B., Kretschmer, F., Sprekeler, H., and Letzkus, J.J. (2020). A thalamocortical top-down circuit for associative memory. Science *370*, 844–848. https://doi.org/10.1126/science.abc2399.
11. Fan, L.Z., Kheifets, S., Böhm, U.L., Wu, H., Piatkevich, K.D., Xie, M.E., Parot, V., Ha, Y., Evans, K.E., Boyden, E.S., et al. (2020). All-optical electrophysiology reveals the role of lateral inhibition in sensory processing in cortical layer 1. Cell *180*, 521–535.e18. https://doi.org/10.1016/j.cell.2020.01.001.
12. Letzkus, J.J., Wolff, S.B.E., Meyer, E.M.M., Tovote, P., Courtin, J., Herry, C., and Lüthi, A. (2011). A disinhibitory microcircuit for associative fear learning in the auditory cortex. Nature *480*, 331–335. https://doi.org/10.1038/nature10674.
13. Shapson-Coe, A., Januszewski, M., Berger, D.R., Pope, A., Wu, Y., Blakely, T., Schalek, R.L., Li, P., Wang, S., Maitlin-Shepard, J., et al. (2021). A connectomic study of a petascale fragment of human cerebral cortex. Preprint at bioRxiv, 10.1101/2021.05.29.446289. https://doi.org/10.1101/2021.1105.1129.446289v446281.
14. Schneider-Mizell, C.M., Bodor, A., Brittain, D., Buchanan, J., Bumbarger, D.J., Elabbady, L., Kapner, D., Kinn, S., Mahalingam, G., Seshamani, S., et al. (2023). Cell-type-specific inhibitory circuitry from a connectomic census of mouse visual cortex. Preprint at bioRxiv. https://doi.org/10.1101/2023.01.23.525290.
15. Fan, L.Z., Kim, D.K., Jennings, J.H., Tian, H., Wang, P.Y., Ramakrishnan, C., Randles, S., Sun, Y., Thadhani, E., Kim, Y.S., et al. (2023). All-optical physiology resolves a synaptic basis for behavioral timescale plasticity. Cell *186*, 543–559.e19. https://doi.org/10.1016/j.cell.2022.12.035.
16. Turner, N.L., Macrina, T., Bae, J.A., Yang, R., Wilson, A.M., Schneider-Mizell, C., Lee, K., Lu, R., Wu, J., Bodor, A.L., et al. (2022). Reconstruction of neocortex: Organelles, compartments, cells, circuits, and activity. Cell *185*, 1082–1100.e24. https://doi.org/10.1016/j.cell.2022.01.023.
17. Huang, Z.J., and Paul, A. (2019). The diversity of GABAergic neurons and neural communication elements. Nat. Rev. Neurosci. *20*, 563–572. https://doi.org/10.1038/s41583-019-0195-4.
18. Scala, F., Kobak, D., Bernabucci, M., Bernaerts, Y., Cadwell, C.R., Castro, J.R., Hartmanis, L., Jiang, X., Laturnus, S., Miranda, E., et al. (2021). Phenotypic variation of transcriptomic cell types in mouse motor cortex. Nature *598*, 144–150. https://doi.org/10.1038/s41586-020-2907-3.
19. Kubota, Y., Karube, F., Nomura, M., and Kawaguchi, Y. (2016). The diversity of cortical inhibitory synapses. Front. Neural Circ. *10*, 27. https://doi.org/10.3389/fncir.2016.00027.
20. Rudy, B., Fishell, G., Lee, S., and Hjerling-Leffler, J. (2011). Three groups of interneurons account for nearly 100% of neocortical GABAergic neurons. Dev. Neurobiol. *71*, 45–61. https://doi.org/10.1002/dneu.20853.

21. Nigro, M.J., Hashikawa-Yamasaki, Y., and Rudy, B. (2018). Diversity and connectivity of layer 5 somatostatin-expressing interneurons in the mouse barrel cortex. J. Neurosci. *38*, 1622–1633. https://doi.org/10.1523/JNEUROSCI.2415-17.2017.

22. Ma, Y., Hu, H., Berrebi, A.S., Mathers, P.H., and Agmon, A. (2006). Distinct subtypes of somatostatin-containing neocortical interneurons revealed in transgenic mice. J. Neurosci. *26*, 5069–5082. https://doi.org/10.1523/JNEUROSCI.0661-06.2006.

23. McGarry, L.M., Packer, A.M., Fino, E., Nikolenko, V., Sippy, T., and Yuste, R. (2010). Quantitative classification of somatostatin-positive neocortical interneurons identifies three interneuron subtypes. Front. Neural Circ. *4*, 12. https://doi.org/10.3389/fncir.2010.00012.

24. Wu, S.J., Sevier, E., Dwivedi, D., Saldi, G.A., Hairston, A., Yu, S., Abbott, L., Choi, D.H., Sherer, M., Qiu, Y., et al. (2023). Cortical somatostatin interneuron subtypes form cell-type-specific circuits. Neuron. https://doi.org/10.1016/j.neuron.2023.05.032.

25. Schuman, B., Machold, R.P., Hashikawa, Y., Fuzik, J., Fishell, G.J., and Rudy, B. (2019). Four unique interneuron populations reside in neocortical layer 1. J. Neurosci. *39*, 125–139. https://doi.org/10.1523/JNEUROSCI.1613-18.2018.

26. Bayraktar, T., Welker, E., Freund, T.F., Zilles, K., and Staiger, J.F. (2000). Neurons immunoreactive for vasoactive intestinal polypeptide in the rat primary somatosensory cortex: morphology and spatial relationship to barrel-related columns. J. Comp. Neurol. *420*, 291–304.

27. Kawaguchi, Y., and Kubota, Y. (1996). Physiological and morphological identification of somatostatin- or vasoactive intestinal polypeptide-containing cells among GABAergic cell subtypes in rat frontal cortex. J. Neurosci. *16*, 2701–2715. https://doi.org/10.1523/JNEUROSCI.16-08-02701.1996.

28. Machold, R., Dellal, S., Valero, M., Zurita, H., Kruglikov, I., Meng, J., Hanson, J.L., Hashikawa, Y., Schuman, B., Buzsáki, G., and Rudy, B. (2022). Id2 GABAergic interneurons: a neglected fourth major group of cortical inhibitory cells. Preprint at bioRxiv. https://doi.org/10.1101/2022.12.01.518752.

29. Markram, H., Muller, E., Ramaswamy, S., Reimann, M.W., Abdellah, M., Sanchez, C.A., Ailamaki, A., Alonso-Nanclares, L., Antille, N., Arsever, S., et al. (2015). Reconstruction and simulation of neocortical microcircuitry. Cell *163*, 456–492. https://doi.org/10.1016/j.cell.2015.09.029.

30. DeFelipe, J., López-Cruz, P.L., Benavides-Piccione, R., Bielza, C., Larrañaga, P., Anderson, S., Burkhalter, A., Cauli, B., Fairén, A., Feldmeyer, D., et al. (2013). New insights into the classification and nomenclature of cortical GABAergic interneurons. Nat. Rev. Neurosci. *14*, 202–216. https://doi.org/10.1038/nrn3444.

31. Jiang, X., Shen, S., Cadwell, C.R., Berens, P., Sinz, F., Ecker, A.S., Patel, S., and Tolias, A.S. (2015). Principles of connectivity among morphologically defined cell types in adult neocortex. Science *350*, aac9462. https://doi.org/10.1126/science.aac9462.

32. Kodandaramaiah, S.B., Flores, F.J., Holst, G.L., Singer, A.C., Han, X., Brown, E.N., Boyden, E.S., and Forest, C.R. (2018). Multi-neuron intracellular recording *in vivo* via interacting autopatching robots. Elife *7*, e24656. https://doi.org/10.7554/eLife.24656.

33. Campagnola, L., Seeman, S.C., Chartrand, T., Kim, L., Hoggarth, A., Gamlin, C., Ito, S., Trinh, J., Davoudian, P., Radaelli, C., et al. (2022). Local connectivity and synaptic dynamics in mouse and human neocortex. Science *375*, eabj5861. https://doi.org/10.1126/science.abj5861.

34. Buxhoeveden, D.P., and Casanova, M.F. (2002). The minicolumn hypothesis in neuroscience. Brain *125*, 935–951. https://doi.org/10.1093/brain/awf110.

35. Sporns, O., Tononi, G., and Kötter, R. (2005). The human connectome: a structural description of the human brain. PLoS Comput. Biol. *1*, e42. https://doi.org/10.1371/journal.pcbi.0010042.

36. Mountcastle, V.B. (1997). The columnar organization of the neocortex. Brain *120* (*Pt 4*), 701–722.

37. Anastasiades, P.G., Collins, D.P., and Carter, A.G. (2021). Mediodorsal and ventromedial thalamus engage distinct L1 circuits in the prefrontal cortex. Neuron *109*, 314–330.e4. https://doi.org/10.1016/j.neuron.2020.10.031.

38. Jones, E.G. (2000). Microcolumns in the cerebral cortex. Proc. Natl. Acad. Sci. USA *97*, 5019–5021. https://doi.org/10.1073/pnas.97.10.5019.

39. Carlo, C.N., and Stevens, C.F. (2013). Structural uniformity of neocortex, revisited. Proc. Natl. Acad. Sci. USA *110*, 1488–1493. https://doi.org/10.1073/pnas.1221398110.

40. Bellmund, J.L.S., Gärdenfors, P., Moser, E.I., and Doeller, C.F. (2018). Navigating cognition: Spatial codes for human thinking. Science *362*, eaat6766. https://doi.org/10.1126/science.aat6766.

41. Ray, S., Naumann, R., Burgalossi, A., Tang, Q., Schmidt, H., and Brecht, M. (2014). Grid-layout and theta-modulation of layer 2 pyramidal neurons in medial entorhinal cortex. Science *343*, 891–896. https://doi.org/10.1126/science.1243028.

42. Zheng, K., Wang, G., Miao, C., Murphy, R., Simonsen, Ø.W., Nilssen, E.S., Miyazaki, K., Ross, W.N., Scott, M.M., Deisseroth, K., et al. (2021). A new commissural mechanism in the medial entorihinal cortex. Soc. Neurosci. Abstr. *23*, P101–P108.

43. Shi, Y., Cui, H., Li, X., Chen, L., Zhang, C., Zhao, X., Li, X., Shao, Q., Sun, Q., Yan, K., and Wang, G. (2023). Laminar and dorsoventral organization of layer 1 interneuronal microcircuitry in superficial layers of the medial entorhinal cortex. Cell Rep. *42*, 112782.

44. van den Heuvel, M.P., and Sporns, O. (2019). A cross-disorder connectome landscape of brain dysconnectivity. Nat. Rev. Neurosci. *20*, 435–446. https://doi.org/10.1038/s41583-019-0177-6.

45. Canter, R.G., Penney, J., and Tsai, L.H. (2016). The road to restoring neural circuits for the treatment of Alzheimer's disease. Nature *539*, 187–196. https://doi.org/10.1038/nature20412.

46. Palop, J.J., and Mucke, L. (2016). Network abnormalities and interneuron dysfunction in Alzheimer disease. Nat. Rev. Neurosci. *17*, 777–792. https://doi.org/10.1038/nrn.2016.141.

47. Bi, D., Wen, L., Wu, Z., and Shen, Y. (2020). GABAergic dysfunction in excitatory and inhibitory (E/I) imbalance drives the pathogenesis of Alzheimer's disease. Alzheimers Dement. *16*, 1312–1329. https://doi.org/10.1002/alz.12088.

48. Aru, J., Suzuki, M., and Larkum, M.E. (2020). Cellular mechanisms of conscious processing. Trends Cognit. Sci. *24*, 814–825. https://doi.org/10.1016/j.tics.2020.07.006.

49. Pardi, M.B., Schroeder, A., and Letzkus, J.J. (2023). Probing top-down information in neocortical layer 1. Trends Neurosci. *46*, 20–31. https://doi.org/10.1016/j.tins.2022.11.001.

50. Takeda, T., Hosokawa, M., and Higuchi, K. (1997). Senescence-accelerated mouse (SAM): a novel murine model of senescence. Exp. Gerontol. *32*, 105–109. https://doi.org/10.1016/s0531-5565(96)00036-8.

51. Cheng, X.R., Zhou, W.X., and Zhang, Y.X. (2014). The behavioral, pathological and therapeutic features of the senescence-accelerated mouse prone 8 strain as an Alzheimer's disease animal model. Ageing Res. Rev. *13*, 13–37. https://doi.org/10.1016/j.arr.2013.10.002.

52. Zhu, Y., and Zhu, J.J. (2004). Rapid arrival and integration of ascending sensory information in layer 1 nonpyramidal neurons and tuft dendrites of layer 5 pyramidal neurons of the neocortex. J. Neurosci. *24*, 1272–1279.

53. Braak, H., Alafuzoff, I., Arzberger, T., Kretzschmar, H., and Del Tredici, K. (2006). Staging of Alzheimer disease-associated neurofibrillary pathology using paraffin sections and immunocytochemistry. Acta Neuropathol. *112*, 389–404. https://doi.org/10.1007/s00401-006-0127-z.

54. Frisoni, G.B., Altomare, D., Thal, D.R., Ribaldi, F., van der Kant, R., Ossenkoppele, R., Blennow, K., Cummings, J., van Duijn, C., Nilsson, P.M., et al. (2022). The probabilistic model of Alzheimer disease: the amyloid hypothesis revised. Nat. Rev. Neurosci. *23*, 53–66. https://doi.org/10.1038/s41583-021-00533-w.

55. Gu, J., Wang, Z., Kuen, J., Ma, L., Shahroudy, A., Shuai, B., Liu, T., Wang, X., Wang, G., Cai, J., and Chen, T. (2018). Recent advances in convolutional neural networks. Pattern Recogn. *77*, 354–377. https://doi.org/10.1016/j.patcog.2017.10.013.

56. Krizhevsky, A., Sutskever, I., and Hinton, G.E. (2017). ImageNet classification with deep convolutional neural networks. Commun. ACM *60*, 84–90. https://doi.org/10.1145/3065386.

57. Pi, H.J., Hangya, B., Kvitsiani, D., Sanders, J.I., Huang, Z.J., and Kepecs, A. (2013). Cortical interneurons that specialize in disinhibitory control. Nature *503*, 521–524. https://doi.org/10.1038/nature12676.

58. Lee, S., Kruglikov, I., Huang, Z.J., Fishell, G., and Rudy, B. (2013). A disinhibitory circuit mediates motor integration in the somatosensory cortex. Nat. Neurosci. *16*, 1662–1670. https://doi.org/10.1038/nn.3544.

59. Zhang, S., Xu, M., Kamigaki, T., Hoang Do, J.P., Chang, W.C., Jenvay, S., Miyamichi, K., Luo, L., and Dan, Y. (2014). Long-range and local circuits for top-down modulation of visual cortex processing. Science *345*, 660–665. https://doi.org/10.1126/science.1254126.

60. Karnani, M.M., Jackson, J., Ayzenshtat, I., Hamzehei Sichani, A., Manoocheri, K., Kim, S., and Yuste, R. (2016). Opening holes in the blanket of inhibition: localized lateral disinhibition by VIP interneurons. J. Neurosci. *36*, 3471–3480. https://doi.org/10.1523/JNEUROSCI.3646-15.2016.

61. Pfeffer, C.K., Xue, M., He, M., Huang, Z.J., and Scanziani, M. (2013). Inhibition of inhibition in visual cortex: the logic of connections between molecularly distinct interneurons. Nat. Neurosci. *16*, 1068–1076. https://doi.org/10.1038/nn.3446.

62. Larkum, M.E., and Zhu, J.J. (2002). Signaling of layer 1 and whisker-evoked Ca^{2+} and Na^{+} action potentials in distal and terminal dendrites of rat neocortical pyramidal neurons *in vitro* and *in vivo*. J. Neurosci. *22*, 6991–7005.

63. Zhu, J.J. (2000). Maturation of layer 5 neocortical pyramidal neurons: amplifying salient layer 1 and layer 4 inputs by Ca^{2+} action potentials in adult rat tuft dendrites. J. Physiol. *526*, 571–587.

64. Larkum, M.E., Zhu, J.J., and Sakmann, B. (1999). A new cellular mechanism for coupling inputs arriving at different cortical layers. Nature *398*, 338–341.

65. Larkum, M. (2013). A cellular mechanism for cortical associations: an organizing principle for the cerebral cortex. Trends Neurosci. *36*, 141–151. https://doi.org/10.1016/j.tins.2012.11.006.

66. Mountcastle, V.B. (1957). Modality and topographic properties of single neurons of cat's somatosensory cortex. J. Neurophysiol. *20*, 404–434.

67. Hubel, D.H., and Wiesel, T.N. (1963). Shape and arrangement of columns in cat's striate cortex. J. Physiol. *165*, 559–568. https://doi.org/10.1113/jphysiol.1963.sp007079.

68. Yu, Y.C., Bultje, R.S., Wang, X., and Shi, S.H. (2009). Specific synapses develop preferentially among sister excitatory neurons in the neocortex. Nature *458*, 501–504.

69. Schröter, M., Paulsen, O., and Bullmore, E.T. (2017). Micro-connectomics: probing the organization of neuronal networks at the cellular scale. Nat. Rev. Neurosci. *18*, 131–146. https://doi.org/10.1038/nrn.2016.182.

70. Yoshiyama, Y., Higuchi, M., Zhang, B., Huang, S.M., Iwata, N., Saido, T.C., Maeda, J., Suhara, T., Trojanowski, J.Q., and Lee, V.M.Y. (2007). Synapse loss and microglial activation precede tangles in a P301S tauopathy mouse model. Neuron *53*, 337–351. https://doi.org/10.1016/j.neuron.2007.01.010.

71. Hartman, R.E., Wozniak, D.F., Nardi, A., Olney, J.W., Sartorius, L., and Holtzman, D.M. (2001). Behavioral phenotyping of GFAP-apoE3 and -apoE4 transgenic mice: apoE4 mice show profound working memory impairments in the absence of Alzheimer's-like neuropathology. Exp. Neurol. *170*, 326–344. https://doi.org/10.1006/exnr.2001.7715.

72. Zheng, J., Li, H.L., Tian, N., Liu, F., Wang, L., Yin, Y., Yue, L., Ma, L., Wan, Y., and Wang, J.Z. (2020). Interneuron accumulation of phosphorylated tau impairs adult hippocampal neurogenesis by suppressing GABAergic transmission. Cell Stem Cell *26*, 331–345.e6. https://doi.org/10.1016/j.stem.2019.12.015.

73. Wang, G., Wyskiel, D.R., Yang, W., Wang, Y., Milbern, L.C., Lalanne, T., Jiang, X., Shen, Y., Sun, Q.-Q., and Zhu, J.J. (2015). An optogenetics- and imaging-assisted simultaneous multiple patch-clamp recordings system for decoding complex neural circuits. Nat. Protoc. *10*, 397–412.

74. Wang, G., Zhang, P., Mendu, S.K., Wang, Y., Zhang, Y., Kang, X., Desai, B.N., and Zhu, J.J. (2020). Revaluation of magnetic properties of Magneto. Nat. Neurosci. *23*, 1047–1050. https://doi.org/10.1038/s41593-019-0473-5.

75. Zhu, J.J. (2009). Activity level-dependent synapse-specific AMPA receptor trafficking regulates transmission kinetics. J. Neurosci. *29*, 6320–6335.

76. Couey, J.J., Witoelar, A., Zhang, S.J., Zheng, K., Ye, J., Dunn, B., Czajkowski, R., Moser, M.B., Moser, E.I., Roudi, Y., and Witter, M.P. (2013). Recurrent inhibitory circuitry as a mechanism for grid formation. Nat. Neurosci. *16*, 318–324. https://doi.org/10.1038/nn.3310.

77. Geiger, J.R.P., Bischofberger, J., Vida, I., Fröbe, U., Pfitzinger, S., Weber, H.J., Haverkampf, K., and Jonas, P. (2002). Patch-clamp recording in brain slices with improved slicer technology. Pflügers Archiv *443*, 491–501.

78. Zhang, L., Zhang, P., Wang, G., Zhang, H., Zhang, Y., Yu, Y., Zhang, M., Xiao, J., Crespo, P., Hell, J.W., et al. (2018). Ras and Rap signal bidirectional synaptic plasticity via distinct subcellular microdomains. Neuron *98*, 783–800.e4. https://doi.org/10.1016/j.neuron.2018.03.049.

79. Brecht, M., Roth, A., and Sakmann, B. (2003). Dynamic receptive fields of reconstructed pyramidal cells in layers 3 and 2 of rat somatosensory barrel cortex. J. Physiol. *553*, 243–265.

80. Shepherd, G.M.G., and Svoboda, K. (2005). Laminar and columnar organization of ascending excitatory projections to layer 2/3 pyramidal neurons in rat barrel cortex. J. Neurosci. *25*, 5670–5679.

81. Manns, I.D., Sakmann, B., and Brecht, M. (2004). Sub- and suprathreshold receptive field properties of pyramidal neurones in layers 5A and 5B of rat somatosensory barrel cortex. J. Physiol. *556*, 601–622.

82. Zhang, Z.W., and Deschênes, M. (1997). Intracortical axonal projections of lamina VI cells of the primary somatosensory cortex in the rat: a single-cell labeling study. J. Neurosci. *17*, 6365–6379.

83. Canto, C.B., and Witter, M.P. (2012). Cellular properties of principal neurons in the rat entorhinal cortex. II. The medial entorhinal cortex. Hippocampus *22*, 1277–1299. https://doi.org/10.1002/hipo.20993.

84. Lim, C.S., Kang, X., Mirabella, V., Zhang, H., Bu, Q., Araki, Y., Hoang, E.T., Wang, S., Shen, Y., Choi, S., et al. (2017). BRaf signaling principles unveiled by large-scale human mutation analysis with a rapid lentivirus-based gene replacement method. Genes Dev. *31*, 537–552. https://doi.org/10.1101/gad.294413.116.

85. Lim, C.S., Wen, C., Sheng, Y., Wang, G., Zhou, Z., Wang, S., Zhang, H., Ye, A., and Zhu, J.J. (2017). Piconewton-scale analysis of Ras-BRaf signal transduction with single-molecule force spectroscopy. Small *13*, 1701972, 10.1002/smll.201701972. https://doi.org/10.1002/smll.201701972.

86. Guan, J.S., Su, S.C., Gao, J., Joseph, N., Xie, Z., Zhou, Y., Durak, O., Zhang, L., Zhu, J.J., Clauser, K.R., et al. (2011). Cdk5 is required for memory function and hippocampal plasticity via the cAMP signaling pathway. PLoS One *6*, e25735. https://doi.org/10.1371/journal.pone.0025735.

STAR★METHODS

KEY RESOURCES TABLE

REAGENT or RESOURCE	SOURCE	IDENTIFIER
Chemicals, peptides, and recombinant proteins		
Biocytin	Sigma-Aldrich	Cat No: 576-19-12
Spermine	Sigma-Aldrich	Cat No: 71-44-3
Sodium phosphocreatine	Sigma-Aldrich	Cat No: 19333-65-4
Na_2ATP	Sigma-Aldrich	Cat No: 987-65-5
MgATP	Sigma-Aldrich	Cat No: 74804-12-9
Na_2GTP	Sigma-Aldrich	Cat No: 36051-31-7
Tetrodotoxin citrate (TTX, Na channel blocker)	Calbiochem	Cat No: 554412
Experimental models: Organisms/strains		
Mouse: C57BL/6	Jackson Laboratory	Stock No: 000664; RRID:IMSR_JAX:000664
Mouse: SAMP8	Envigo (formerly Harlan)	Stock No: SAMP8/TaHsd RRID:IMSR_ENV:HSD-954
Software and algorithms		
Igor Pro 6	Wavemetrics	http://www.wavemetrics.com/
PEPOI; an Igor-based operation and analysis program for simultaneous Electrophysiology, Optogenetics & Imaging experiments	Home-made[73]	Contact UVA Patent Foundation (https://lvg.virginia.edu/) for the end user license
Neurolucida	BMF Bioscience	https://www.mbfbioscience.com/products/neurolucida/
Multiple simultaneous automatic patch-clamp procedures integrated in the remote control $SM10^{touch}$ system	Luigs & Neumann GmbH	https://www.luigs-neumann.org/

RESOURCE AVAILABILITY

Lead contact

Further information and requests for resources and reagents can be directed to and will be fulfilled by Dr. Julius Zhu (jjzhu@virginia.edu).

Materials availability

This study did not generate unique reagents.

Data and code availability

- All data reported in this paper will be shared by the lead contact upon request.
- The original codes for data generation and analysis will be shared by the lead contact upon request. These codes have also been deposited and publicly available at University of Virginia Patent Foundation and/or Luigs & Neumann GmbH as of the date of publication. The links to access are listed in the key resources table.
- Any additional information required to reanalyze the data reported in this paper is available from the lead contact upon request.

EXPERIMENTAL MODEL AND SUBJECT PARTICIPANT DETAILS

Adult male and female C57BL/6J and senescence-accelerated mouse prone 8 (SAMP8) mice (≥ postnatal 42-*d*ay-old or P42) were used in this study. The animals were housed in the animal facilities under controlled conditions. They were kept in a temperature-

controlled room with a 12-h light and 12-h dark cycle. Food and water were available *ad libitum*. All procedures for animal surgery and maintenance were performed following protocols approved by the Animal Care & Use Committee of the University of Virginia and in accordance with US National Institutes of Health guidelines.

METHOD DETAILS

Parallel brain slice preparation

Decoding complex neuronal circuits often requires the analysis of large datasets of neurons and their synaptic connections. This analysis is most effectively conducted using brain tissue slice or tissue block preparations.[3,4,13] Simultaneous whole-cell patch-clamp recording method is advantageous over high-speed electron microscopy in deciphering functional neuronal circuits. However, unlikely optogenetic approaches, the patch-clamp method requires the presence of all elements of the circuit in single tissue slices. Hence, we focused our effort on preparing the healthiest slices that preserved sufficient neurons and their connections. Acute cortical slices were made from ~2 to 10-month old animals following our previous studies.[63,74] In brief, animals were deeply anesthetized by xylazine-ketamine, decapitated, and then the brain was quickly removed and placed into cold (0−4°C) oxygenated physiological solution containing (in mM): 125 NaCl, 2.5 KCl, 1.25 NaH_2PO_4, 25 $NaHCO_3$, 1 $MgCl_2$, 25 dextrose, and 2 $CaCl_2$, pH 7.4. Different slicing techniques were employed to optimize the preparation process. For the motor-prefrontal and somatosensory cortical slices, the mouse brain was severed into two hemispheres with a straight middle cut, and then, the right brain hemisphere was laid down on a ramp with an angle of 22° or 27° in a slicing chamber, respectively.[63,75] The entorhinal cortical slices were made by optimizing a previous preparation.[76] Specifically, separation of the right brain hemisphere was made with a cut at an angle of 9° along the anterior-posterior axis and an angle of 4.5° along the dorsal-ventral axis, and the right brain hemisphere was then laid down on the flat bottom of the slicing chamber. Horizontal or sagittal brain slices 400-μm thick were cut from the hemispheres with a microslicer (DTK-1000; Dosaka, Kyoto, Japan), which is essential for preparing healthy tissue slices.[77]

Typically, 4–5 brain slices were collected, and incubated at 37.0 ± 0.5°C in oxygenated physiological solution for ~30−60 min prior to recordings. Visual inspection was made to select one brain slice that retained intact apical dendrites of large layer 5–6 (**L5-6**) pyramidal neurons in L1-2. This slice, with the dendrites (and axons) best aligned to the slice surface and thus more intact transsynaptic circuits retained, was chosen for the experiment. Nevertheless, it is important to acknowledge that slice sectioning amputated a significant amount of neuronal connections, leading to underestimated connectivity values reported in the study. During the recording, the slices were submerged in a chamber and stabilized with a fine nylon net attached to a platinum ring.

Electrophysiology

Simultaneous whole-cell patch-clamp *in vitro* recordings were obtained as previously described.[5,6] Briefly, patch recording pipettes (4−7 MΩ) were filled with intracellular solutions containing (mM): 135 cesium methanesulfonate, 10 HEPES, 2.5 $MgCl_2$, 4 Na_2ATP, 0.4 Na_3GTP, 10 sodium phosphocreatine, 0.6 EGTA, 0.1 spermine and 0.5% biocytin, at pH 7.25 for current recordings, or 120 potassium gluconate, 10 HEPES, 4 KCl, 4 MgATP, 0.3 Na_2GTP, 10 sodium phosphocreatine and 0.5% biocytin, at pH 7.25, for voltage recordings. The recording system consisted of eight Axopatch 200B and/or Axoclamp 2A/B amplifiers (Molecular Devices, Sunnyvale, CA), eight JUNIOR Compact motorized manipulators (Lugis & Neumann Feinmechanik and Elektrotechnik, Ratingen, Germany). The recording system was interfaced with two ITC-18 interface boards (HEKA Instruments Inc, Bellmore, NY) and multiple DAQ boards (National Instruments Corporation, Austin, TX) custom-modified to achieve simultaneous A/D and D/A conversions of current, voltage, and command and triggering signals for eight amplifiers, as well as operational control of eight motorized manipulators and a Zeiss microscope.

In the recorded neurons, the presynaptic single action potential-evoked uIPSCs or uIPSPs in >4-week old cortical neurons were highly reliable and often exhibited no transmission failure. This reliability enabled the unambiguous identification of inhibitory synaptic connections after online monitoring of the average responses of short-latency uIPSPs for ≥20 episodes.[5,6] Unless otherwise specified, IPSCs and IPSPs were measured with membrane potentials of postsynaptic cells clamped or held at −55 mV and −55 ± 3 mV, respectively. Recording traces shown were typically averages of 20–200 consecutive episodes.

Octuple-sexdecuple recording system

To develop a system capable of handling ≥10 neurons, we initially incorporated 16 Luigs and Neumann JUNIOR Compact manipulators (Luigs and Neumann GmbH, Ratingen, Germany), which was minimized to 49 mm in width,[73] in our recording system. Yet, our tests proved this design ineffective because including >8 manipulators in the setup congested the working space, which made the task more challenging and prone to human errors. Additionally, the increased setup complexity led to longer recording times required to obtain individual recordings, which averaged from ~6 to 8 min in an octuple setup to ~8−11 min in a sexdecuple setup. Frequently, after obtaining patch-clamp recordings from the ~10^{th} neurons, the first-recorded neurons and/or brain slices started to deteriorate, leaving little time for rigorous connectivity analysis.

To address these challenges, we reset the system back to eight manipulators and implemented an alternative sequential recording strategy to record ≥10 neurons (cf.[62]). We developed automatic procedural algorithms to operate microscope and manipulators. Iterative algorithm evolution optimized automatic procedures, which performed image analysis, identified suitable neurons for targeted recording, assigned targeted neurons to appropriate manipulators (with optimized approaching angles), set up recording

orders, and positioned patch electrodes next to targeted neurons. Investigators manually performed the delicate gigasealing step, as it demanded rapid and experienced reactions to accommodate the diverse neuronal responses to the approaching and gigasealing of patch pipettes.

The filling of patch pipettes with internal solution was facilitated by with semiautomatic apparatuses developed previously,[63] and the replacement of pipettes was assisted by the Luigs and Neumann ultra-stable guide-rail electrode exchange system.[73] This hybrid automatic and manual recording system optimized high-throughput and high-quality, reducing the average time of obtaining recordings from individual cells to ~3–5 min (cf.[32]). Importantly, this system maintained high success rates of high-quality whole-cell recordings from interneurons (>95%), and stellate and pyramidal neurons (>99%). Quantitative analysis showed no difference in connectivity measurements between the initial and sequential multiple recordings (Figure S7, cf; [63,78]), validating the effectiveness of octuple–sexdecuple patch-clamp recording system. The mechanical, electronic, and algorithmic improvements pertaining to the octuple–sexdecuple patch-clamp recording method have been communicated to Luigs and Neumann GmbH in Germany. The company has enhanced and incorporated these ideas into their user-friendly SM10^{touch} system, aiming to the dissemination of the technique within the broader research community.

Morphology reconstruction

Light microscopic examination followed our previous procedures.[5,6] In brief, after *in vitro* recordings, the slices were fixed by immersion in 3% acrolein/4% paraformaldehyde in 0.1 M PBS at 4°C for 24 h, and subsequently processed with the avidin-biotin-peroxidase method to reveal cell morphology. Morphologically recovered cells were examined, drawn, and analyzed with the aid of a microscope equipped with a 100× oil immersion objective and a computerized reconstruction system Neurolucida (BMF Bioscience, Williston, VT). Recent taxonomy has classified cortical cells into a very large number of neuron groups, yet it remains unclear whether the choice represents biologically[17] or functionally[18] discrete entities. Here, we grouped recorded neurons into the traditionally described cortical cell types and layers based on the established criteria.[29,79–83] More than 85% of recorded interneurons and 95% of recorded excitatory neurons had their axonal arborization largely recovered and could thus be unambiguously classified into these general cortical cell groups.

Behavioral analysis

Fear conditioning and Morris water maze paradigm tests are conducted following our previous protocols.[84–86] Briefly, the standard fear conditioning is performed in an isolated shock chamber (Coulbourn Instruments, Wilmette, IL). The standard fear conditioning training consists of a 3 min exposure of mice to the conditioning box (context) followed by a foot shock (2 s, 0.8 mA) after a preceding tone (30 s, 3 kHz, 75 dB). The memory test is performed 24 h later by re-exposing the animals for 5 min to the conditioning context. The water maze with hidden platform paradigm is performed in a circular tank (diameter 1.8 m) filled with opaque water. A platform (11 × 11 cm) is submerged below the water's surface in the center of the target quadrant. For each training trial, the mice are placed into the maze consecutively from one of four random points of the tank. During the memory test (probe test), the platform is removed from the tank, and the mice are allowed to swim in the maze for 60 s. These behavioral tests are imaged, and analyzed offline with fully automated MTALAB-based algorithms.

QUANTIFICATION AND STATISTICAL ANALYSIS

Statistical analysis

All results were reported as mean ± sem. Animals, slices, or cells were randomly assigned, and investigators are blinded to experiment treatments to minimize bias. Based on the effect size d calculated from previous and preliminary data, the sample size was estimated to be $\geq$~8–25/group to attain the desired power of $\geq$80% with statistical significance set as $\alpha < 0.05$. Statistical significance of the means was determined using non-parametric tests such as Wilcoxon and Mann-Whitney Rank Sum for paired and non-paired samples, respectively. Chi-squared tests were used for categorical data. Statistical significance of the linear relationships of two data groups was determined using linear regression *t* test ($p < 0.05$) provided the normality and constant variance tests passed. The data collected from male and female animals were compared to explore possible sex-dependent differences. All the data were pooled together for final analysis since no difference was detected. For the animals used for the behavioral tests, they were subsequently prepared for the electrophysiology study as well. Additional animals were included specifically for the electrophysiology experiments. The electrophysiological data obtained from animals with and without the behavioral tests were pooled together for final analysis since no difference was detected.